Microfabricated Quadrupole Mass Spectrometer with a Brubaker Pre-filter

by

S. Wright[1], S.O'Prey[1], R.R.A. Syms[2]*, G.Hong[1], A.S. Holmes[2]

Abstract

Microfabricated quadrupole mass spectrometers with Brubaker pre-filters are demonstrated for the first time. Complete filters are assembled from two dies, each carrying two pairs of rods providing the pre-filter and main filter sections. The rods are held in precision silicon mounts that are fabricated using wafer scale deep reactive ion etching and anodic bonding to glass substrates. Improvements to ion transmission are obtained by tuning the bias potential applied to the pre-filter. The effect is explained in terms of a simple analytic theory for ion motion in the pre-filter. Mass filtering with a range of m/z = 0-1200 and a resolution of $m/\Delta m \approx 150$ at 10% of peak height is demonstrated using 2-4 mm long pre-filter electrodes, 30 mm long main electrodes (both of 650 μm diameter) and a RF drive at ≈ 6.5 MHz.

KEYWORDS: Mass spectrometry, Quadrupole filter, Prefilter, MEMS

[1]Microsaic Systems Ltd., Unit 2, GMS House, Boundary Road, Woking, Surrey, GU21 5BX, UK

[2]Optical and Semiconductor Devices Group, EEE Dept., Imperial College, Exhibition

Road,

London SW7 2AZ, UK

*Corresponding Author

TEL +44-207-594-6203 FAX +44-207-594-6308 email r.syms@imperial.ac.uk

1. Introduction

The quadrupole mass filter, originally introduced by Paul [1], is a workhorse of analytical mass spectrometry, since it may easily be constructed without the need for a magnet. Its operation is well-understood [2-4]. The device consists of a set of four parallel electrodes, arranged to create a hyperbolic electrostatic field as shown in Figure 1a. Often the ideal hyperbolic electrodes are approximated by cylinders of radius r_e [5], with the ratio between r_e and the radius of an inscribed circle r_0 being chosen to optimise performance [6, 7].

Ions are injected into a pupil between the electrodes as shown in Figure 1b, and travel parallel to them for a distance L_F under the influence of a time-varying field that contains both direct current (DC) and alternating current (AC) components. It can be shown that only ions near a particular mass-to-charge ratio will transit without discharging on a rod, and if the voltage amplitudes are ramped, the time variation of the output is a mass spectrum. Resolution is determined by the accuracy with which the field is created, the number of AC cycles experienced by each ion, and the ratio between the DC and AC voltages. Highly accurate construction is required to achieve an adequate analytical performance. The ions are injected with a small axial velocity, a radio frequency (RF) drive is used, and the voltage ratio is chosen to operate near the peak of a so-called ‘first stability zone’ [2-4].

Sensitivity is primarily limited by the ion flux. Since the flux reduces as the size of the pupil is decreased, this aspect is clearly of importance to small mass spectrometers. However, sensitivity is also strongly reduced at high resolution, due to the perturbing effect of the fringing field at the filter entrance caused by the exposed ends of the electrodes. In this region, the field is no longer purely hyperbolic and in addition contains axial components. In 1967, Brubaker proposed a simple solution, namely to precede the filter with a short set of quadrupole electrodes or 'stubbies' of length L_P carrying only AC voltages, as shown in Figure 1c [8]. The prefilter can be driven from the main filter via capacitors, using additional resistive pathways to ground to leak away any accumulated charge. Experimentally, very large improvements in transmission have been observed at high resolution, albeit accompanied by mass-dependent transmission oscillations [9, 10].

The pre-filter is itself a form of quadrupole known as an 'RF-only quadrupole' [10, 11]. Such a device has its own set of detailed ion dynamics, which may be explained in terms of a confining potential well or 'pseudopotential' created by an inhomogeneous time-varying electric field [12]. At low pressures, RF-only quadrupoles can be used for guiding or transporting ions, at higher pressures for additionally forcing ions towards the instrument axis by collision focusing [13, 14], and at higher pressures still for fragmentation of ions by collision with a neutral gas [15]. The motion of ions through the pre-filter and into main-filter is complicated, and has so far mainly been understood in terms of detailed numerical simulations of trajectories [16, 17].

In recent years, considerable efforts have been devoted to miniaturisation of most types of mass filter to allow portable or desktop applications [18-21]. Particular attention has been devoted to cylindrical ion traps (CITs), since these may be easily constructed as planar arrays [22-25], and several portable systems containing CITs have been demonstrated [26-29]. More recently, microfabricated ion traps have been demonstrated in cylindrical [30-33], toroidal [34] and linear [35-37] arrangements. Many other mass filter types have been realised in microfabricated form, including magnetic and crossed field filters [38-43], time-of-flight filters [44-48] and ion separators based on travelling electric fields [49, 50].

Quadrupole filters have been relatively difficult to miniaturise, since their features are not amenable to fabrication by surface processing alone. Their size has been reduced to the mm-scale using conventional engineering [51], and small quadrupole arrays have been constructed to increase sensitivity [52-54]. Unconventional fabrication methods, such as the LIGA process, have also been investigated for 100 micron-scale quadrupole arrays [55].

The most promising results have, however, been obtained from devices of intermediate size constructed using silicon-based microfabrication. Quadrupoles have been formed from two closely spaced, stacked Si substrates, each containing pairs of 0.5 mm dia in-plane cylindrical electrodes rigidly fixed in V-grooves [56-59]. Similar array-type devices have also been proposed [60]. Taking advantage of the increased complexity offered by bonded silicon-on-insulator (BSOI), quadrupoles have been formed from two BSOI substrates that hold electrodes in grooves with micromachined springs [61, 62].

The latter arrangement has been used in portable and desktop mass spectrometers [63]. Alternative arrangements have used pairs of widely spaced substrates carrying out-of-plane cylindrical electrodes [64, 65], and in-plane arrangements of etched rods with rectangular cross-section, operated in a higher stability zone [66]. The performance of microfabricated quadrupoles is steadily improving, but constructional accuracy has limited resolution, the maximum tolerated RF voltage has restricted mass range, and small size has restricted sensitivity.

One way to increase ion transmission in microfabricated quadrupoles would be to incorporate a pre-filter. Unfortunately, none of the approaches above is appropriate due to the relatively short length of the filter electrodes. Out-of-plane constructions would clearly require complex stacked assemblies. In-plane approaches are potentially more suitable, but the V-groove construction in [56-59] suffers from RF coupling through the Si substrate, while the spring mounting used in [61, 62] is not easily adaptable to short electrodes.

In this paper, an enhancement to all major performance criteria of an in-plane microfabricated quadrupole is demonstrated, by incorporating a Brubaker pre-filter using an advanced fabrication process based on silicon-on-glass. The silicon parts are defined by deep reactive etching [67, 68] and attached to Pyrex by anodic bonding [69, 70] using methods previously developed for capacitive sensors [71] and vacuum packages [72]. The fabrication process is designed to improve yield by mounting the main electrodes on strain-relieved supports that reduce damage caused by thermal expansion mismatch. The use of glass substrates is designed to reduce RF coupling, so that higher voltages may be applied and the mass range increased. Finally, the incorporation of a pre-filter is designed to increase transmission at high resolution.

A simple explanation of pre-filter operation is presented in Section 2 in terms of an analytic theory of ion motion. The design and fabrication of the microfabricated filter are described in Section 3. Mass filtering experiments are presented in Section 4, and a mass range of $m/z = 0\text{-}1200$ is demonstrated with a mass resolution of $m/\Delta m \approx 150$ at 10% of peak height using a RF drive at $\approx$ 6.5 MHz. The effects most commonly seen using a Brubaker pre-filter (namely an overall improvement in ion transmission, coupled with energy dependent transmission effects) are all observed, and the experimental behaviour is correlated to the earlier theoretical analysis. Finally, conclusions are drawn in Section 5.

2. Ion motion in quadrupole filters and prefilters

In general the performance of quadrupole devices can only be understood from a detailed simulation of ion motion. Normally large numbers of ion trajectories are integrated, using a finite element model of the electric fields that can incorporate fringe fields and coupling to an ion source [16, 17]. Here the important features are highlighted using a simple analytic theory for non-interacting ions, assuming ideal hyperbolic fields.

Electrostatic field and equations of motion

The geometry is shown in Figure 1. Assuming that axial and transverse motions are un-coupled and the axial energy is V_A, the axial velocity v_A of an ion of mass m and charge e is:

$$v_A = (2eV_A/m)^{1/2} \tag{1}$$

The axial position z may then be related to time t as $z = v_A t$. Transverse motion is governed by the electric field distribution shown in Figure 1a. Assuming that the electrodes carry potentials ± $\phi_0/2$, the result is a two-dimensional potential field:

$$\phi(x, y) = \phi_0(x^2 - y^2)/2r_0^2 \tag{2}$$

Here r_0 is the radius of a circle touching the equipotentials $\phi = \pm \phi_0/2$. For an ion moving in the z-direction, the equations of motion in the x- and y-directions are:

$$m\, d^2x/dt^2 = -e\partial\phi/\partial x = -e\phi_0 x/r_0^2$$

$$m\, d^2y/dt^2 = -e\partial\phi/\partial y = +e\phi_0 y/r_0^2$$

(3)

Main filter operation

In the main filter, the applied voltage contains both DC and AC components, so that the time variation of the potential may be written as $\phi_0(t) = U - V \cos[\omega(t - t_0)]$, where $\omega = 2\pi f$ is an angular frequency, ωt_0 is the starting phase of the ion and U and V are constant potentials. In this case, the equations of motion reduce to:

$$d^2x/dt^2 + (e/mr_0^2)\ \{U - V \cos[\omega(t - t_0)]\}\ x = 0$$

$$d^2y/dt^2 - (e/mr_0^2)\ \{U - V \cos[\omega(t - t_0)]\}\ y = 0$$

(4)

Using the substitutions $\zeta = \omega t/2$, $\zeta_0 = \zeta(0)$, $a = 4eU/(m\omega^2 r_0^2)$ and $q = 2eV/(m\omega^2 r_0^2)$, Equations 4 can be reduced to the Matthieu-like equations:

$$d^2u/d\zeta^2 + \{a_u - 2q_u \cos[2(\zeta - \zeta_0)]\}\ u = 0$$

(5)

Where u is x or y, and $a = a_x = -a_y$ and $q = q_x = -q_y$.

It can be shown (see e.g. ref. [3]) that the nature of the trajectory depends almost entirely on a and q, varying little with the initial conditions u(0) and u'(0) and the starting phase ζ_0. There are several regions on the q-a plane that give rise to bounded, stable solutions. The lower stability region is an approximately triangular region, bounded by the lines:

$$a_0(q) = q^2/2 - 7q^4/128 + 29q^6/2304 \ldots.$$
$$b_1(q) = 1 - q - q^2/8 + q^3/64 - q^4/1536 - 11q^5/36864 \ldots. \tag{6}$$

The line a_0 defines the stability limit for trajectories in the y-direction, while b_1 is the similar limit in the x-direction. Between the two, trajectories are stable in both directions. The apex of the stable region lies at a = 0.23699, q = 0.70600, so that U/V = a/2q = 0.1678.

Figure 2a shows example x-trajectories obtained by numerical integration of Equations 5, calculated assuming that x(0) = 1, x'(0) = 0, $\zeta_0 = 0$, q = 0.706 and a/2q = 0.1671 (thick line) and a/2q = 0.1675 (thin line). These two conditions lie just below the apex of the stability region. In each case, the motion involves rapid oscillations, whose amplitudes first slowly increase and then slowly decrease, so that the trajectory is bounded. However, for a/2q = 0.1675 the apex of the stable region is approached more closely and the peak ion displacement is larger. Consequently, although the trajectory remains stable in this case, ions must be injected closer to the axis to transit successfully. Since the ions are injected as a relatively broad beam, overall transmission is therefore likely to fall. As an extension, it may be assumed that perturbations to the direction of ions travelling close to the axis caused by fringe fields will also reduce transmission.

In operation, U and V are normally ramped together, following an operating line passing just below the apex of the lower stability region of different masses as shown in Figure 2b. Stable trajectories are then only obtained for a narrow mass range, so that the device acts as a scanning mass filter, with the filtered mass being determined from the AC voltage as $m = 2eV/(q\omega^2 r_0^2)$. The use of a scan line passing close to the stability tip requires that the voltage ratio U/V be just less than 0.1678, with the mass resolution increasing as this value is approached. However, the discussion above implies that there is a trade-off between ion transmission and resolution, with the former falling as the latter rises. Based only on the width of the stable region, the mass resolution $m/\Delta m$ can be estimated as [3]:

$$m/\Delta m = 0.1256 / \{0.1678 - U/V\} \tag{7}$$

However, resolution is strongly affected by other factors, such as the number of RF cycles experienced by the ion, and constructional accuracy.

Pre-filter operation

In the pre-filter, the DC voltage is omitted, so that the equations of motion reduce to:

$$d^2u/d\zeta^2 - 2q_u \cos[2(\zeta - \zeta_0)]\, u = 0$$

(8)

This simplification causes a change in behaviour, which may conveniently be discussed in terms of a simple approximation developed for time varying, inhomogeneous fields [12]. The approximate solution is found by assuming that ion trajectories consist of a large mean trajectory $\xi_0(\zeta)$ combined with small oscillations $\xi_1(\zeta) \cos[2(\zeta - \zeta_0)]$ at the RF frequency. In this case, the complete ion displacement may be written as:

$$u(\zeta) = \xi_0(\zeta) + \xi_1(\zeta) \cos[2(\zeta - \zeta_0)]$$

(9)

Differentiating this solution, but assuming that derivatives of ξ_1 can be neglected, yields:

$$d^2u/d\zeta^2 \approx d^2\xi_0/d\zeta^2 - 4\xi_1 \cos[2(\zeta - \zeta_0)]$$

(10)

Substituting Equations 9 and 10 into 8, but noting that $\cos^2(\theta) = \{1 + \cos(2\theta)\}/2$, yields:

$$d^2\xi_0/d\zeta^2 - 4\xi_1 \cos[2(\zeta - \zeta_0)] - 2q_u\xi_0 \cos[2(\zeta - \zeta_0)] - q_u\xi_1\{1 + \cos[4(\zeta - \zeta_0)]\} = 0$$

(11)

Separately equating the constant terms and the coefficients of $\cos[2(\zeta - \zeta_0)]$, but neglecting the term involving $\cos[4(\zeta - \zeta_0)]$ in Equation 9) then gives:

$$d^2\xi_0/d\zeta^2 - q_u\xi_1 = 0 \quad \text{and} \quad \xi_1 = -q_u\xi_0/2$$

(12)

Verification that neglect of the higher-order term is reasonable (at least, within the limits of the initial approximation) can be achieved by including an additional term $\xi_2(\zeta)$ $\cos[4(\zeta - \zeta_0)]$ in the assumed solution (9) and showing that its coefficient is small.

Finally, combining Equations 12 shows that the mean trajectory is governed by the second order differential equation:

$$d^2\xi_0/d\zeta^2 + (q_u^2/2)\xi_0 = 0 \tag{13}$$

Since $q_u^2/2$ is constant, Equation 13 describes simple harmonic motion, and implies that the ion will oscillate to-and-fro in form of potential well known as a ‘pseudopotential’, which is proportional to the square of the applied RF voltage. The general solution for $\xi_0(\zeta)$ is:

$$\xi_0(\zeta) = A\cos(q_u\zeta/\sqrt{2}) + B\sin(q_u\zeta/\sqrt{2}) \tag{14}$$

Equation 14 describes a sinusoidal trajectory with a constant amplitude and a period determined by the value of q_u, with a larger period being obtained at smaller q_u. Equation 12 implies in turn that the amplitude of the faster oscillations is not constant, but depends on the mean trajectory, so that the complete solution $u(\zeta)$ is:

$$u(\zeta) = \{A\cos(q_u\zeta/\sqrt{2}) + B\sin(q_u\zeta/\sqrt{2})\}\{1 - (q_u/2)\cos[2(\zeta - \zeta_0)]\} \tag{15}$$

Although the period of the oscillation is the same for all ions, the exact trajectory depends on the coefficients A and B, which must be obtained from the boundary conditions. For example, for ions injected parallel to the axis at a distance u(0) from the axis, A and B are:

$$A = u(0)/\{1 - (q_u/2)\cos(2\zeta_0)\}$$

$$B = A\sqrt{2}\,\sin(2\zeta_0)/\{1 - (q_u/2)\cos(2\zeta_0)\} \qquad (16)$$

In this case, Figure 3a shows comparisons between the exact solution (Equation 8), the approximate solution (Equation 15) and the mean trajectory (Equation 14) for x-trajectories obtained with $\zeta_0 = 0$ and $q = 0.35$. Here, the exact and approximate solutions are in excellent agreement. The period of the main oscillation is large, the amplitude of the faster superimposed oscillation is small and the mean trajectory is a good representation of the overall motion. When q rises (for example towards 0.706), the agreement becomes less good, since the exact solution predicts a smaller mean period and larger superimposed oscillations. However, despite this discrepancy, qualitatively similar behaviour is obtained.

The operation of a Brubaker pre-filter may now be understood in broad terms as follows. Firstly, it provides an improvement in transmission by minimising the effects of DC fringe fields at the sensitive input to the main filter. Secondly, it provides a guiding effect on the input ions, whose trajectories are forced by the pseudopotential to have an inherent periodicity.

When q is sufficiently small, Equation 12 implies that ξ_1 will be negligible. Only the slow oscillations need be considered, and the solution is mainly described by Equations 14 and 16. Since the coefficient B is strongly dependent on the starting phase ζ_0, ions entering at different times must follow different trajectories. In particular, because B > A, ions entering near $\zeta_0 = \pi/4$ will make larger maximum excursions. However, whenever the sin term in Equation 14 vanishes the effect of the phase disappears. This condition occurs when

$$q_u\zeta/\sqrt{2} = \mu\pi, \text{ where } \mu = 1, 2 \ldots \tag{17}$$

The result is illustrated in Figure 3b, which shows exact ion trajectories calculated for different values of ζ_0 equally distributed between 0 and π, assuming that $q = 0.35$. The trajectories are significantly different, with much larger maximum excursions in some cases. However, all trajectories return together when $\zeta/\pi = \sqrt{2}/0.35 \approx 4.04$, $\zeta/\pi = 8.08$ and so on. In the former case, the pre-filter is effectively forming an inverted image of the input ion distribution, and in the latter case a real image. Integrating over all possible starting conditions in both x and y directions as was done by Trajber [16, 17], the average diameter of the ion beam will clearly be smaller at the image conditions. If this point coincides with the start of the main filter, further benefits in transmission might be expected, since ions will then be injected optimally through the DC fringe fields.

Substituting $\zeta = \omega t/2$, $t = L_P/v_A$ and $v_A = (2eV_A/m)^{1/2}$ into Equation 17 yields the axial ion energy V_A required to reach each of these image-forming conditions as:

$$1/V_A^{1/2} = 2\mu(e/m)^{1/2}/(qfL_P) \tag{18}$$

Equation 18 now implies that mass-dependent transmission effects would be expected at fixed energy. Alternatively, fluctuations in transmission with energy would be expected for a fixed mass, so that a plot of $1/V_A^{1/2}$ against the peak number μ should be a straight line.

To minimise the rate at which transmission changes with energy or mass, μ should be small. For example, if $\mu \approx 1$, the pre-filter will operate near its primary image-forming condition and quite large changes in mass will be needed to reach the second one. To achieve a small value of μ, either a large axial ion energy V_A or a short pre-filter length L_P is required. Large ion energies are undesirable, because small velocities are required for high resolution in the main filter. Consequently, L_P is normally small. However, it cannot be too small, or the advantages of fringe-field screening will be lost. The exact choice is therefore a compromise, with L_P typically being taken to be around the electrode diameter [8]. Unfortunately, in MEMS devices, there are difficulties with handling very short rods, and we have therefore investigated somewhat longer pre-filters. Similarly, the exact choice of separation between the electrodes in the two filter sections is a compromise. The gap cannot be too large, or fringe-fields will again be an issue. However, it cannot be too small or breakdown may occur. The gap is therefore normally taken as a small fraction of the electrode diameter. Once again, there are additional difficulties in MEMS devices with reliably achieving small gaps and those used here were the minimum compatible with repeatable alignment.

The pre-filter length L_P is then normally a small fraction of the main filter length L_F. If both sections are directly coupled and driven using DC and RF, the combination acts as a marginally longer main filter. It might be expected, therefore, that some of the beneficial effect of the capacitively coupled, RF-only pre-filter will be masked by the improved resolution afforded by the longer, directly coupled combined filter. However, Equation 6.3 in [3] shows that, given the stated operating parameters, the ultimate resolution is not limited in the present case by the number of cycles. Hence, this difference in filter length is of no consequence.

Departures from the predictions above are to be expected at high resolution, as q will then be large, or whenever the assumption of a parallel input beam is inappropriate, for example when the size of the entrance pupil is large compared with the exit pupil of the ion source.

3. Design and fabrication

Experience with early microfabricated quadrupoles has shown that accurate construction using materials appropriate for RF operation at up to several hundred volts is essential for high resolution. Previous comparable devices have used dies formed from oxidised silicon or bonded-silicon-on-insulator to mount cylindrical electrode rods formed from metallised glass or stainless steel. Problems are then caused by the temperature rise that follows from RF heating within the semiconducting substrate, because the mismatch in thermal expansion coefficient of the electrodes and silicon causes die deformation and/or electrode detachment. Electrical loss also makes it difficult to achieve sufficiently high voltage from the RF drive.

Design

Here we introduce a new approach based on silicon-on-glass, which provides improved electrical, mechanical and thermal performance. The complete mass filter is constructed from a pair of microfabricated dies, each carrying half of the electrode rods. Figure 4a shows a single die, which provides microfabricated silicon mounts for pairs of pre-filter and main filter electrodes on a glass substrate. Here the aspect ratio has been reduced for clarity. The short pre-filter electrodes are mounted in single fixed silicon feature as shown in Section A-A’ of Figure 4b. However, the longer main filter electrodes must be held at each end. To allow differential thermal expansion with respect to the glass substrate, which otherwise tends to bend the substrate, one end of each electrode is held in a fixed feature, while the other is mounted in a spring feature formed as a suspended portal frame as shown in Section B-B'. Associated with axial motion of the electrodes is a quadratically varying transverse motion that tends to separate their movable ends. Over a temperature range of (say) 100^{o}, the transverse motion is sub-micron for the flexure length used. Because this deflection is small compared with other dimensional tolerances, its effect on performance has not been quantified. However, since it varies quadratically with the inverse of flexure length, it could easily be reduced by design. The effect of thermal expansion between the electrodes and the very much shorter contact regions on the silicon parts is assumed to be small enough to allow attachment using conductive epoxy.

Silicon features also provide mounts for precision alignment spacers, which allow two such substrates to be aligned together in three orthogonal directions so that the combined set of electrodes forms a quadrupole as shown in Figure 5a. The dimensions of the electrode mounting fixtures can be calculated using the quadrant geometry shown in Figure 5b. For example, the distance s between the electrode centres and the ion optical axis is $s = \{r_e + r_0\}/2^{1/2}$. If the distance between the two contact points of the cylindrical electrode and the groove in the supporting feature is 2w, the height h between the contact points and the axis of symmetry is $h = s + (r_e^2 - w^2)^{1/2}$. Suitable choices of r_e, r_0, s, w and h therefore allow the geometry of a quadrupole to be established. Other key dimensions such as the flexure widths and lengths can be chosen to provide suitable thermal compliance.

Fabrication

Devices were fabricated using a high-yield, wafer-scale batch process based on 100 mm diameter wafers of silicon and Pyrex glass as shown in Figure 6. The Si wafers were 400 μm thick, (100) oriented and D/S polished and thermally matched to the glass wafers, which were typically 500 μm thick Pyrex 7740 type. The silicon was repetitively patterned by mid UV photolithography using a Quintel IR 4000 contact mask aligner equipped with through-wafer infrared illumination, and etched using a Surface Technology Systems Single-Chamber Multiplex inductively coupled plasma etcher operating a cyclic etch-passivate process based on SF_6 and C_4F_8 gases (the Bosch process). In each case, AZ9260 photoresist was used for patterning, and a silicon etch rate of 1 μm/min was used for deep etching. Residual resist was stripped using an Oxford Plasma Technology System 80 RIE.

Three layers of patterning were used. The rear side silicon was first etched to a shallow depth to define anchor points for electrode mounts and form shallow recesses to allow subsequent motion of the suspended parts (Step 1). The main outlines of the electrode mounts were then partially defined using a second etch (Step 2). The wafer was then anodically bonded to a Pyrex wafer at the anchors, using an aligner-bonder (Step 3). A conducting surface layer was then provided on the front side using layers of Cr and Au metal deposited using a Nordiko RF sputter coater with thicknesses of 30 nm and 100 nm respectively (Step 4). The metals were patterned by lithography and wet chemical etching first in potassium iodide and then in ceric ammonium nitrate (Step 5). The front side silicon was then etched to complete the definition of the electrode mounts and form alignment trenches for the electrode rods (Step 6). In some variants, holes were formed in the glass prior to bonding, to allow access to electrodes. However, completed wafers were entirely robust. Figure 7a shows a completed silicon-on-glass-wafer, before dicing. A variety of filter variants may be seen, each comprising a set of electrically isolated silicon parts on a glass backing, together with additional test structures. Finally, the wafer was mechanically diced using a rotary saw to yield dies of approximately 7 mm in width and 34 mm in length (Step 7), and the electrode rods were attached using conductive epoxy (Step 8).

Metal-coated glass electrodes have previously been used by one of the present authors [56], and these can have reduced mismatch in thermal expansion coefficient. However, they are tedious to fabricate, since at least two coating cycles of each of two metals (an adhesion layer and a conductor) are required to avoid breaks in the film. Stainless steel electrodes are simpler to source, and the elastic suspension then provides an effective solution to thermal mismatch.

Stainless steel electrode rods were purchased pre-cut with a diameter of 650 μm. The rod ratio was $r_e/r_0 \approx 1.14$, and lengths of either 2 mm or 4 mm were used for the pre-filter and 30 mm for the main filter. After cleaning, the rods were inserted unto their respective alignment grooves and attached using conductive epoxy. Rods were inserted manually and their longitudinal positions were adjusted under a microscope. Epoxy was again applied manually and its amount was verified under the same microscope.

The design separation between the two filter sections was 80 μm. Using 80 measurements taken from 20 devices, the average axial separation between the pre-filter and main filter electrodes was determined as 79.1 μm, with a standard deviation of 10.3 μm. Similarly, using 40 measurements taken from 10 devices, the average axial displacement between two rod ends on the same die (measured for the main rod at the pre-filter end) was determined as 5.3 μm with a standard deviation of 5.6 μm.

No damage to the flexible electrode suspensions was observed, despite the use of mechanical handling during assembly and thermal curing for the attachment epoxy. Connections were then made to the electrode mounts using gold wire and conductive epoxy. A second die was then stacked on top of the first, using the precision alignment spacers, and connections from the top die were then brought down to a small PCB sub-mount. Figure 7b shows an assembled filter. The pre-filter is on the left, and the main filter on the right, and the electrode rods may be seen running along the centre of the device.

4. Evaluation

Performance of completed devices was evaluated using an electron impact ion source and analytes that give well-separated mass peaks over a wide mass range. The overall aim was to demonstrate the advantages of using a silicon-on-glass technology and incorporating a pre-filter with respect to improved mass range, resolution and transmission.

Experimental arrangement

Mass filters were evaluated in a stainless steel vacuum test rig pumped by a 130 ls^{-1} turbo pump and equipped with a cold cathode pressure gauge. Filters were mounted on stainless steel flanges equipped with electrical feed-throughs, between an electron-impact ion source and a channeltron electron multiplier used for ion detection.

The ion source is similar to the well-known VG Anavac source. It is designed for use with a much larger quadrupole filter (6 mm dia rods), and consequently produces a relatively large ion beam. The exit pupil of the final electrode of the ion source was therefore reduced to match the inscribed circle of the microfabricated filter. The ion energy in the main filter was determined from the voltage applied to the source cage, as the bias applied to the main rods was 0 V throughout. A Detech 2120 channeltron (Detector Technology Inc.) operated in pulse counting mode was used to detect the ions.

RF waveforms were supplied to the mass filter under computer control by custom electronics. The two out-of-phase RF signals required to drive the filter sections were supplied by a resonant amplifier driven by a HP 33120A signal generator. Frequencies in the range 6.2 - 6.9 MHz were used, depending on the exact device configuration. A DC command voltage (0-10 V) was used to set the RF amplitude during a scan. The pre-filter rods were coupled to the main rods using 100 pF capacitors. Any bias voltage was applied to the pre-filter pairs through high-value resistors. The fraction of the RF component coupled to the pre-filter is close to unity, as the impedance of the capacitors is small compared with the bias resistors.

Mass range

Mass spectra were obtained for perfluorotributylamine or PFTBA ($C_{12}F_{27}N$, molecular weight 671.09), and tris(perfluoroheptyl)-s-triazine ($C_3N_3[(CF_2)_6CF_3]_3$, molecular weight 1185.22). PFTBA is often used to calibrate mass spectrometers fitted with EI sources. It has a relatively high vapour pressure at room temperature, and was therefore held in a stainless steel phial located outside the vacuum system and connected to it by a leak valve. After pumping away the air above the sample, PFTBA was admitted to the vacuum chamber to a pressure of 5×10^{-7} Torr. Tris(perfluoro-heptyl)-s-triazine is also used for calibration, particularly for instruments with a high mass range. It is a solid at room temperature, and has a low vapour pressure. A small amount (20 mg) was placed in a stainless steel cup directly in front of the ion source, where it sublimed at a rate sufficient to raise the chamber pressure to between 5×10^{-7} and 1×10^{-6} Torr.

Figures 8 and 9 show mass spectra for the two compounds, obtained using devices equipped with 4mm and 2 mm pre-filter electrodes, respectively. In each case, the ion energy was V_A = 2 eV and no pre-filter bias was used. These spectra were acquired over 10 minutes in both cases and represent multiple summed scans. The acquisition period was chosen so as to give good-signal-to-noise levels for the smallest peaks in the spectra. The larger peaks can all be seen in a single scan (acquired in less than 30 seconds). Figure 8a shows a measured spectrum for PFTBA, and Figure 8b shows for comparison a reference spectrum from the National Institute of Standards and Technology (NIST) mass spectral database [72]. High-mass portions of the experimental data are shown plotted using expanded intensity scales. The reference spectrum is clearly well reproduced by the microfabricated filter and the mass scale is linear. There are some discrepancies in relative peak heights (for example, the relatively low peak at m/z = 219). One explanation may be the mass-dependent ion transmission effects investigated below. However, resolved peaks may be seen up to m/z = 614. Figures 9a and 9b show experimental data and a NIST reference spectrum for tris(perfluoroheptyl)-s-triazine. Here, mass peaks can be seen up to almost m/z = 1200, and the very small peak at m/z =1185 (shown in detail later on) indicates successful detection of the molecular ion. At 1200 a.m.u., the maximum voltage between adjacent rods was 770 V. These results represent an approximate trebling of the mass range obtained in [59, 60], and confirm the benefits of the improved electrical properties of glass substrates.

Mass resolution

Figure 10a shows the variation of the mass resolution m/Δm (defined as the mass of the ion divided by the width of the peak, either at 10% or 50% of peak height) with the voltage ratio U/V, measured at the m/z = 219 peak of PFTBA. The mass resolution rises steeply as the peak of the first stability zone is approached. Also shown in Figure 10a is the theoretical prediction for the variation of resolution, as given in Equation 7. The experimental data are in good agreement with the theory, suggesting that the fields in the quadrupole filter are reasonably close to ideal.

The beneficial effects of the pre-filter can be seen in the peak shapes. Figure 10b shows plots of the m/z = 614 peak of PFTBA obtained using a range of U/V values and an ion energy of 4 eV. When the pre-filter is capacitively coupled to the main filter and receives only the RF component of the waveform, the peak shape is uniform and collapses towards the high mass side as the resolution increases. However, when the pre-filter is directly coupled and fringing fields are reintroduced at the entrance to the filter, the peak shapes become asymmetric and collapse towards the high mass shoulder as the resolution increases.

Ion transmission

Typically, the ion transmission of any quadrupole filter will fall as the resolution increases. For a well-constructed filter, transmission normally reduces quasi-linearly with resolution, when transmission is plotted on a logarithmic scale. However, at a maximum resolution that is often defined by some form of constructional imperfection (for example, misalignment of an electrode rod), transmission typically falls much more rapidly. The variation of transmission with resolution may even double back on itself, and hence set a practical limit to the performance of the filter.

Figure 11a shows the variation of transmission with resolution at 10% of peak height, for the m/z = 219 and 502 peaks of PFTBA. A best resolution of $m/\Delta m \approx 140$ is achieved, which represents an approximate doubling of the resolution reported in [62]. The effect of the pre-filter on the performance is demonstrated in Figure 11b. Two sets of data are shown. The hollow points show results obtained using capacitive coupling of the drive voltages to the pre-filter electrodes. In agreement with Figure 11a, the maximum resolution is ≈ 140. The solid points show corresponding results obtained with direct coupling of the drive voltages to the pre-filter electrodes. In this case, both sets of electrodes carry both DC and AC, and the device effectively acts as a slightly longer quadrupole. The maximum resolution achieved is 115, and the signal intensity is reduced by up to an order of magnitude. These results are qualitatively similar to the original findings of Brubaker [8], who showed that a RF-only pre-filter could increase transmission at a given mass, or alternatively increase the maximum resolution.

Figure 12 shows expanded views of tris(perfluoroheptyl)-s-triazine peaks near m/z = 866 and m/z = 1166, obtained using 2 eV axial ion energy using a device with 2 mm pre-filter electrodes. In Figure 12a, the peak width at 10% of peak height is 6.2 a.m.u., giving a mass resolution of $m/\Delta m \approx 140$. In Figure 10b, the peak width is 7 a.m.u., giving $m/\Delta m \approx 165$. The corresponding values at 50% of peak height are 350 and 360, respectively. These results confirm that a good mass resolution may be obtained over the whole of the mass range. Figure 12b also shows an expanded view of the molecular ion peak.

Transmission oscillations

Experience with macroscopic quadrupoles suggests that mass-dependent transmission effects will arise with a pre-filter, which can cause inaccuracy in measurements of relative ion abundance. This possibility was investigated for the microfabricated device, using PFTBA. The ion source cage voltage was fixed, the main filter was set to pass ions of a particular mass peak, and the ion transmission was measured as a function of a bias voltage applied to the pre-filter electrodes. 22 MΩ bias resistors were used to ensure that the AC amplitude applied to the pre-filter was closely tied to the AC voltage on the main filter.

Figure 13a shows results obtained for the peak at m/z = 219, for different U/V ratios. For each value of U/V, aperiodic oscillations in transmission can be seen, with the oscillation period reducing and overall transmission falling as the bias reduces. However, the locations of the peaks and troughs tend to particular values as U/V rises and the peak of the stability zone is reached. The oscillations are significant. If the bias is set to a value coincident with a trough, the signal can be attenuated by as much as 50%. However, as can be seen in Figure 9, if the bias is coincident with a peak, the transmission can be increased six-fold. Measurements carried out for other ions showed similar transmission oscillations, albeit with different peak and trough locations. To improve mass spectral fidelity, the bias voltage should be ramped as the mass spectrum is scanned, so that it is maintained at an optimum value for each mass. However, the large bias resistor introduces a time constant that restricts the rate of scanning. This limitation is unimportant in applications involving a long acquisition time, or in single ion monitoring.

The elementary theory of ion focusing in an RF-only quadrupole presented in Section 2 suggested that, if the peak locations are determined by particular values of V_A, a plot of $1/V_A^{1/2}$ against μ, where μ is the peak number, should be a straight line with a slope $2(e/m)^{1/2}/(qfL_P)$. Figure 13b shows the variation V_A with μ obtained at the different masses indicated. The straight lines are the theoretical estimates, calculated assuming that $q = 0.706$ (the peak of the first stability zone), $f = 6.4$ MHz and $L_P = 4$ mm, to correspond to the device used, and the discrete data points show measured results. The qualitative agreement is excellent, confirming the earlier interpretation of pre-filter operation and suggesting that the overall behaviour of the microfabricated device is indeed as expected. The rapidity of the transmission oscillations should reduce as the length of the pre-filter section is reduced, and certainly a reduction in L_P down to $\approx$1 mm seems entirely practical.

5. Conclusions

A new technology for microfabricated quadrupole mass filters has been developed using an advanced silicon-on-glass process based on a combination of deep reactive ion etching and anodic bonding. A wafer-scale batch fabrication process for quadrupole filter dies has been demonstrated that yields precision alignment features for pairs of electrode rods and spacers in the form of electrically isolated, metallised silicon parts on glass substrates. Stainless steel electrode rods are inserted into silicon mountings and complete filters are assembled as a stacked combination of two dies separated by spacers. The improved electrical isolation of glass allows an inherently larger mass range than previous filters constructed on silicon and bonded silicon substrates, and a mass range of 0-1200 a.m.u. has been demonstrated with a resolution of ≈ 150 at ≈ 6.5 MHz frequency, the best performance of any form of microfabricated mass filter to date. The technology supports the incorporation of multiple electrode sections, allowing advantage to be taken of the improved transmission obtained when a short RF-only pre-filter is combined with a main filter. Many of the characteristics of macroscopic pre-filters have been observed, including improved transmission at high resolution and mass-dependent transmission. These improvements in performance suggest that benchtop mass spectrometers based on microfabricated filters are now a realistic possibility.

6. Acknowledgements

The Authors are extremely grateful for the support and encouragement of Mr Peter Edwards and Mr Alan Finlay, and the technical assistance of Mr Andrew Malcolm. The assistance of Applied Microengineering Ltd. with wafer bonding and Loadpoint with wafer dicing is also gratefully acknowledged.

7. References

1. W. Paul, and H. Steinwedel, “Ein neues massenspektrometer ohne magnetfeld,” *Z. für Naturforschung* Vol. 8a, pp. 448-450, 1953.
2. J. H. Batey, "Quadrupole gas analysers," *Vacuum* Vol. 37, pp. 659-668, September 1987.
3. P. H. Dawson, *Quadrupole mass spectrometry and its applications*. Amsterdam: Elsevier Scientific Pub. Co., 1976.
4. P. H. Dawson, “Quadrupole mass analyzers: performance, design and some recent applications,” *Mass Spect. Rev.* vol. 5, pp.1-37, March 2005.
5. P. H. Dawson and N. R. Whetten, “Quadrupole mass filter: circular rods and peak shapes,” *J. Vac. Sci. Technol.* vol. 7, pp. 440-441, May 1970.
6. J. R. Gibson and S. Taylor, “Numerical investigation of the effect of electrode size on the behaviour of quadrupole mass filters,” *Rapid Comm. in Mass Spect.* vol. 15, pp. 1960-1964, October 2001.
7. D. J. Douglas and N. V. Konenkov, “Influence of the 6th and 10th spatial harmonics on the peak shape of a quadrupole mass filter with round rods,” *Rapid Comm. in Mass Spect.* vol. 16, pp. 1425-1431, June 2002.
8. W. M. Brubaker, “An improved quadrupole mass analyzer,” *Adv. Mass. Spect.* vol. 4, pp. 293-299, 1968.
9. W. Arnold, “Influence of segmented rods and their alignment on the performance of a quadrupole mass spectrometer,” *J. Vac. Sci. Technol.* vol. 7, pp. 191-194, January 1970.

10. P. E. Miller and D. M. Bonner Denton, “The transmission properties of an RF-only quadrupole mass filter,” *Int. J. Mass Spect.* vol. 72, pp. 223-238, March 1986.
11. P. H. Dawson, “Performance characteristics of an RF-only quadrupole,*” Int J. Mass Spect. Ion Proc.* vol. 67, pp. 267-276, March 1985.
12. D. Gerlich, “Inhomogeneous RF fields: a versatile tool for the study of processes with slow ions,” in *Adv. Chem. Phys. Ser*. Vol LXXXII, *State-selected and State-to-state Ion-molecule Reaction Dynamics. Part 1: Experiment*, C. Y. Ng and M. Baer, Eds. New York: John Wiley and Sons, 1992.
13. D. J. Douglas and J. B. French, “Collision focusing effects in radio-frequency quadrupoles,” *J. Am. Soc. Mass Spect.* vol. 3, pp. 398-408, May 1992.
14. A. V. Tolmachev, I. V. Chernushevich, A. F. Dodonov, and K. G. Standing, “A collision focusing ion guide for coupling an atmospheric pressure ion source to a mass spectrometer,” *Nucl. Instrum. Meth. Phys Res.* vol. B124, pp. 112-119, April 1997.
15. D. Gerlich, “Application of RF fields and collision dynamics in atomic mass spectrometry,” *J. Anal. At. Spect.* vol. 19, pp. 581-590, May 2004.
16. C. Trajber, M. Simon, and M. Csatlos, “On the use of prefilters in quadrupole mass spectrometers,” *Meas. Sci. Technol*. vol. 2, pp. 785-787, August 1991.
17. C. Trajber, M. Simon, and S. Bohatka, “A method for uniform optimisation of quadrupole prefilters,” *Rapid Comm. in Mass Spect.* vol. 6, pp. 459-462, April 1992.
18. E. R. Badman, and R. G. Cooks, “Special feature: Perspective - miniature mass analysers,” *J. Mass. Spect.* vol. 35, pp. 659-671, June 2000.
19. R. R. A. Syms,“Miniaturized mass spectrometers,” presented at 59th Ann. Pittsburgh

Conf. on Analytical Chemistry and Applied Spectroscopy, New Orleans, Luisiana, 2008.

20. Z. Ouyang, and R. G. Cooks, “Miniature mass spectrometers,” *Annual Rev. Anal. Chem.* vol. 2, pp. 10.1-10.28, July 2009.
21. R. R. A. Syms, “Advances in microfabricated mass filters*,” Anal. Bioanal. Chem.* vol. 393, pp. 427-429, January 2009.
22. R. G. Brewer, R. G. Devoe, and R. Kallenbach,“Planar ion microtraps,” *Phys. Rev. A* vol. 46, pp. R6781-R6784, November 1992.
23. J. M. Wells, E. R. Badman, and R. G. Cooks, "A quadrupole ion trap with cylindrical geometry operated in the mass-selective instability mode," *Anal. Chem.* vol. 70, pp. 438-444, January 1998.
24. O. Kornienko, P. T. A. Reilly, W. B. Whitten, and J. M. Ramsey, "Micro ion trap mass spectrometry," *Rapid Comm. in Mass Spect.* vol. 13, pp. 50-53, January 1999.
25. E. R. Badman, and R. G. Cooks, “A parallel miniature cylindrical ion trap array*,” Anal. Chem.* vol. 72, pp. 3291-3297, May 2000.
26. G. E. Patterson, et al., “Miniature cylindrical ion trap mass spectrometer,” *Anal. Chem.* vol. 74, pp. 6145-6153, November 2002.
27. O. J. Orient, and A. Chutjian, “A compact, high-resolution Paul ion trap mass spectrometer with electron-impact ionization,” *Rev. Sci. Inst.* vol. 73, pp. 2157-2160, May 2002.
28. A. M. Tabert, J. Griep-Raming, A. J. Guymon, and R. G. Cooks, “High-throughput miniature cylindrical ion trap array mass spectrometer,” *Anal. Chem.* vol. 75, pp. 5656-5664, November 2003.

29. M. Yang, T.Y. Kim, H.-C. Hwang, S.-K. Yi, and D.-H. Kim, “Development of a palm portable mass spectrometer,” *J. Am. Soc. Mass Spect.* vol. 19, pp. 1442-1448, October 2008.

30. M. G. Blain, et al. “Towards the hand-held mass spectrometer: design considerations, simulation, and fabrication of micrometer-scaled cylindrical ion traps*,” Int. J. Mass Spect.* vol. 236, pp. 91-104, August 2004.

31. S. Pau, at al., “Microfabricated quadrupole ion trap for mass spectrometer applications,” *Phys. Rev. Lett.* vol. 96, Art. 120801, March 2006.

32. F. H. W. Van Amerom, A. Chaudhary, M. Cardenas, J. Bumgarner, and R. T. Short, “Microfabrication of cylindrical ion trap mass spectrometer arrays for handheld chemical analyzers,” *Chem. Eng. Comm.* vol. 195, pp. 98-114, February 2008.

33. A. Chaudhary, F. H. W. Van Amerom, and R. T. Short, “Development of microfabricated cylindrical ion trap mass spectrometer arrays,” *J. Microelectromech. Syst.* vol. 18, pp. 442-448, April 2009.

34. D. E. Austin et al., “Halo ion trap mass spectrometer,” *Anal. Chem.* vol. 79, pp. 2927-2932, March 2007.

35. M. J. Madsen, W. K. Hensinger, D. Stick, J. A. Ratschuk, and C. Monroe, “Planar ion trap geometry for microfabrication,” *Appl. Phys. B-Lasers* vol. O78, pp. 639-651, March 2004.

36. D. Stick, et al. “Ion trap in a semiconductor chip*,” Nature Physics* vol. 2, pp. 36-39, January 2006.

37. M. Brownnutt, G. Wilpers, P. Gill, R. C. Thompson, and A. G. Sinclair, “Monolithic microfabricated ion trap chip design for scaleable quantum processors,” *New J. Phys.*

vol. 8, p. 232, October 2006.

38. C. B. Freidhoff, “Mass spectrograph on a chip,” *in Proc. 1997 IEEE Aerospace Conference*, 1997, p. 32.
39. C. B. Freidhoff, et al., "Chemical sensing using non-optical microelectromechanical systems," *J. Vac. Sci. and Technol.* vol. A17, pp. 2300-2307, July 1999.
40. J. A. Diaz, C. F. Giese, and W. R. Gentry, “Sub-miniature E x B sector-field mass spectrometer,” *J. Am. Soc. Mass Spect.* vol. 12, pp. 619-632, June 2001.
41. J. A. Diaz, P. Daley, R. Miles, H. Rohrs and D. Polla, “Integration test of a miniature ExB mass spectrometer with a gas chromatograph for development of a low-cost, portable, chemical detection system” *Trends in Analytical Chemistry* vol. 23, pp. 314-321, April 2004.
42. N. Sillon, and R. Baptist, “Micromachined mass spectrometer” *Sensors and Actuators* vol. B83, pp. 129-137, March 2002.
43. K. H. Gilchrist, et al., “A novel ion source and detector for a miniature mass spectrometer,” in *Proc. IEEE Sensors Conf.,* 2007, pp 1372-1375.
44. H. J. Yoon, J. H. Kim, T. G. Park, S. S. Yang, and K. W. Jung, “The test of hot emission for the micro mass spectrometer,” *Proc. SPIE* vol. 4408, pp. 360-367, April 2001.
45. H. J. Yoon, J. H. Kim, E. S. Choi, S. S. Yang, and K. W. Jung, “Fabrication of a novel micro time-of-flight mass spectrometer,” Sensors and Actuators vol. A97-8, pp. 441-447, April 2002.
46. J. S. Hwang, et al., “The micro mass spectrometer with a carbon nanostructure ion source” in *Proc. 1st IEEE Int. Conf. on Nano/Micro Engineered and Molecular*

Systems, 2006, pp 1220-1223.

47. G. F. Verbeck, R. Saini, J. W. Wylde, K. Tsui, and M. Ellis, "MEMS assembled mass spectrometry: A novel approach to miniaturization and construction of electron and ion optics," presented at *54th ASMS Conf. on Mass Spectrometry*, Seattle, WA, 2006.
48. E. Wapelhorst, J.-P. Hauschild, and J. Müller, "Complex MEMS: a fully integrated TOF micro mass spectrometer," Sensors and Actuators vol. A138, pp. 22-27, April 2007.
49. P. Siebert, G. Petzold, A. Hellenbart, and J. Müller, "Surface microstructure/miniature mass spectrometer: processing and applications," *Appl. Phys.* vol. A67, pp. 155-160, August 1998.
50. J.-P. Hauschild, E. Wapelhorst, and J. Müller, "Mass spectra measured by a fully integrated MEMS mass spectrometer," *Int. J. Mass Spect*. vol. 264, pp. 53-60, May 2007.
51. D. H. Holkeboer, T. L. Karandy, F. C. Currier, L. C. Frees, and R. E. Ellefson, "Miniature quadrupole residual gas analyser for process monitoring at milliTorr pressures*," J. Vac. Sci. Technol.* vol. A16, pp. 1157-1162, May 1998.
52. R. J. Ferran, and S. Boumsellek, "High pressure effects in miniature arrays of quadrupole analyzers for residual gas analysis from 10^{-9} to 10^{-2} Torr*," J. Vac. Sci. Technol.* vol. A14, pp. 1258-1264, May/June1996.
53. O. J. Orient, A. Chutjian, and V. Garkanian, "Miniature, high-resolution, quadrupole mass-spectrometer array," *Rev. Sci. Instrum.* vol. 68, pp. 1392-1397, March 1997.
54. S. Boumsellek, and R. J. Ferran, "Tradeoffs in miniature quadrupole designs*," J. Am. Soc. Mass Spect.* vol. 12, pp. 633-640, June 2001.

55. D. Wiberg, et. al., “LIGA fabricated two-dimensional quadrupole array and scroll pump for miniature gas chromatograph/mass spectrometer,” *Proc. SPIE* vol. 4878, pp. 8-13, December 2003.
56. R. R. A. Syms, T. J. Tate, M. M. Ahmad, and S. Taylor, "Fabrication of a microengineered quadrupole electrostatic lens," *Elect. Lett.* vol. 32, pp. 2094-2095, October1996.
57. S. Taylor, J. J. Tunstall, R. R. A. Syms, T. J. Tate, and M. M. Ahmad, "Initial results for a quadrupole mass spectrometer with a silicon micromachined mass filter," *Elect. Lett.* vol. 34, pp. 546-547, March 1998.
58. R. R. A. Syms, T. J. Tate, M. M. Ahmad, and S. Taylor, "Design of a microengineered quadrupole electrostatic lens," *IEEE Trans. on Electron Devices* vol. TED-45, pp. 2304-2311, November 1998.
59. S. Taylor, et al., “Performance improvements for a miniature quadrupole with a micromachined mass filter,” *Vacuum* vol. 53, pp. 203-206, May 1999.
60. L. Lebel, L. F. Velasquez-Garcia, and A. I. Akinwande, “Arrays of microfabricated quadrupole mass filters,” in *Tech. Dig. 18th Int. Vacuum Nanoelectronics Conf.*, 2005, pp 366-367.
61. M. Geear, R. R. A. Syms, S. Wright, and A. S. Holmes, “Monolithic MEMS quadrupole mass spectrometers by deep silicon etching” *J. Microelectromech. Syst.* vol. 14, pp. 1156-1166, October 2005.
62. S. Wright, R. R. A. Syms, S. O’Prey, G. Hong, and A. S. Holmes, “Comparison of ion coupling strategies for a microengineered quadrupole mass spectrometer*,” J. Am. Soc. Mass Spect.* vol. 20, pp. 146-156, January 2009.

63. A. Finlay, R. R. A. Syms, S. Wright, and A. Malcolm, "Microsaic Ionchip: the first commercially available mass spectrometer chip," presented *at 57th Ann. Pittsburgh Conf. on Analytical Chemistry and Applied Spectroscopy*, Orlando, FLA, 2006.
64. L. F. Velasquez-Garcia, and A. I. Akinwande, "An out-of-plane MEMS quadrupole for a portable mass spectrometer," *in Proc. Transducers Conf.*, 2007, pp 2315-2320.
65. L. F. Velasquez-Garcia, K. Cheung, and A. I. Akinwande, "An application of 3D MEMS packaging: out-of-plane quadrupole mass filters," J. Microelectromech. Syst. vol. 17, pp.1430-1438, December 2008.
66. K. Cheung, L. F. Velasquez-Garcia, and A. I. Akinwande, "First principles optimization of mass produced microscaled linear quadrupoles for operation in higher stability regions" in *Tech. Dig. 20th IEEE Int. Vacuum Nanoelectronics Conf.*, 2007, pp 214-215.
67. M. Esashi, M. Takinami, Y. Wakabayashi, and K. Minami, "High rate directional deep dry etching for bulk silicon micromachining," *J. Micromech. Microeng*. vol. 5, pp. 5-10, March 1995.
68. A. M. Hynes, et al., "Recent advances in silicon etching for MEMS using the ASE™ process," *Sensors and Actuators* vol. 74, pp. 13-17, April 1999.
69. T. Rogers, "Considerations of anodic bonding for capacitive type silicon/glass sensor fabrication," *J. Micromech. Microeng*. vol. 2, pp. 164-166, September 1992.
70. A. Cozma, and B. Puers, "Characterization of the electrostatic bonding of silicon and Pyrex glass," *J. Micromech. Microeng*. vol. 5, pp. 98-102, June 1995.
71. M. Esashi, N. Ura, and Y. Matsumoto, "Anodic bonding for integrated capacitive sensors," in *Proc. MEMS '92*, 1992, pp 43-48.

72. H. Henmi, S. Shoji, Y. Yoshimi, and M. Esashi, “Vacuum packaging for microsensors by glass-silicon anodic bonding,” *Sensors and Actuators* vol. A43, pp. 243-248, May 1994.

73. Mass Spectral Library, National Institute of Standards and Technology, Gaithersburg, MD, USA

8. Figures

1. a) Hyperbolic electrostatic field; b) quadrupole, and c) quadrupole with pre-filter.
2. a) Example x-trajectory in a main filter, calculated assuming that $q = 0.706$, $\zeta_0 = 0$ and $a/2q = 0.1671$ (thick line) and $a/2q = 0.1675$ (thin line); b) the shape of the first stability zone, plotted on the V – U plane for different masses.
3. a) Example x-trajectories in a pre-filter, calculated assuming that $\zeta_0 = 0$ and $q = 0.35$. Thick lines show the exact solution, thin lines show the approximate solution, and dashed lines show the mean trajectory. b) Exact trajectories, calculated assuming $q = 0.35$ and assuming different starting phases $\zeta_0 = \nu\pi/8$ with $\nu = 0, 1, \ldots 7$.
4. a) Plan and b) section view of microfabricated quadrupole die with Brubaker pre-filter.
5. a) Quadrupole assembly; b) geometry for calculation of rod mount design parameters.
6. Process flow for device fabrication.
7. a) Silicon-on-glass wafer, before dicing; b) assembled quadrupole filter with prefilter.
8. Mass spectrum of perfluorotributylamine, a) as obtained using a microfabricated quadrupole with pre-filter, and b) from the NIST reference library.
9. Mass spectrum of tris(perfluoroheptyl)-s-triazine, a) as obtained using a microfabricated quadrupole with pre-filter, and b) from the NIST reference library.
10. a) Variation of resolution ($m/\Delta m$) at 10% of peak height with U/V ratio. Points are experimental data for 10% and 50% of peak height; line is theory. b) Peak shapes obtained for nominal $m/z = 614$ with an axial ion energy of 4 eV and different U/V ratios, with capacitive (L) and direct (R) coupling to the pre-filter

11. a) Variation of ion transmission with mass resolution for m/z = 219 and m/z = 502, with capacitive coupling of the pre-filter and an axial ion energy of 2 eV. b) Variation of ion transmission with resolution, for direct (solid data points) and capacitive (hollow data points) coupling of the pre-filter electrodes to the main electrodes. In each case, data were obtained for the m/z = 614 peak of PFTBA, using different axial ion energies.
12. High resolution mass spectra for tris(perfluoroheptyl)-s-triazine, measured near a) m/z = 866 and b) m/z = 1166, using 2 eV axial ion energy.
13. a) Variation of ion transmission with pre-filter bias voltage, measured for the m/z = 219 peak of PFTBA for different U/V ratios as detailed on the legend; b) variation of V_A with μ for the transmission maxima obtained for different fragment ions of PFTBA. Points are experimental data, lines are theory.

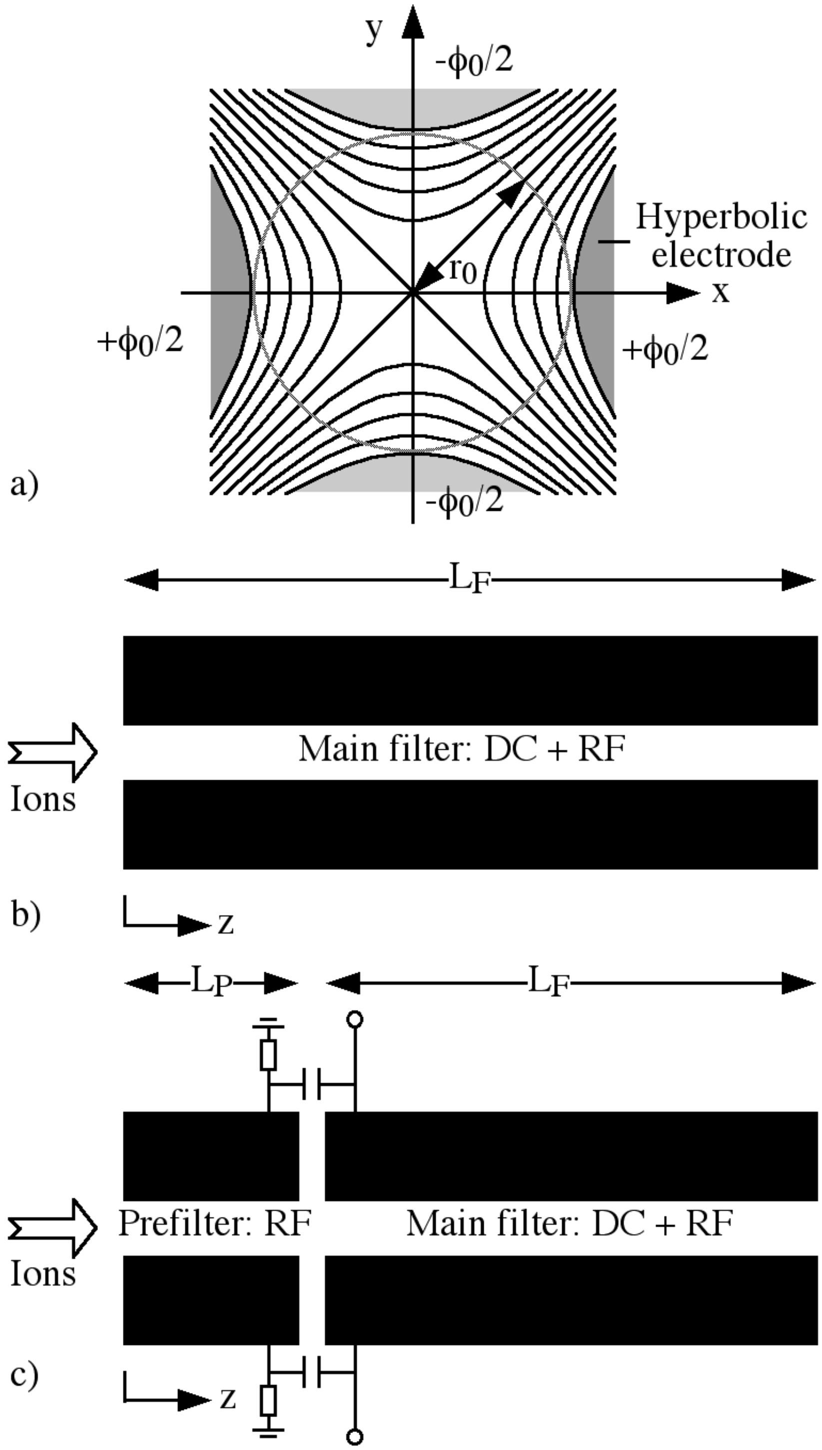
y
-ϕ0/2
Hyperbolic
electrode
r0
x
+ϕ0/2
+ϕ0/2
-ϕ0/2
a)
LF
Main filter: DC + RF
Ions
b)
z
LP
LF
Prefilter: RF
Main filter: DC + RF
Ions
c)
z

Figure 1.

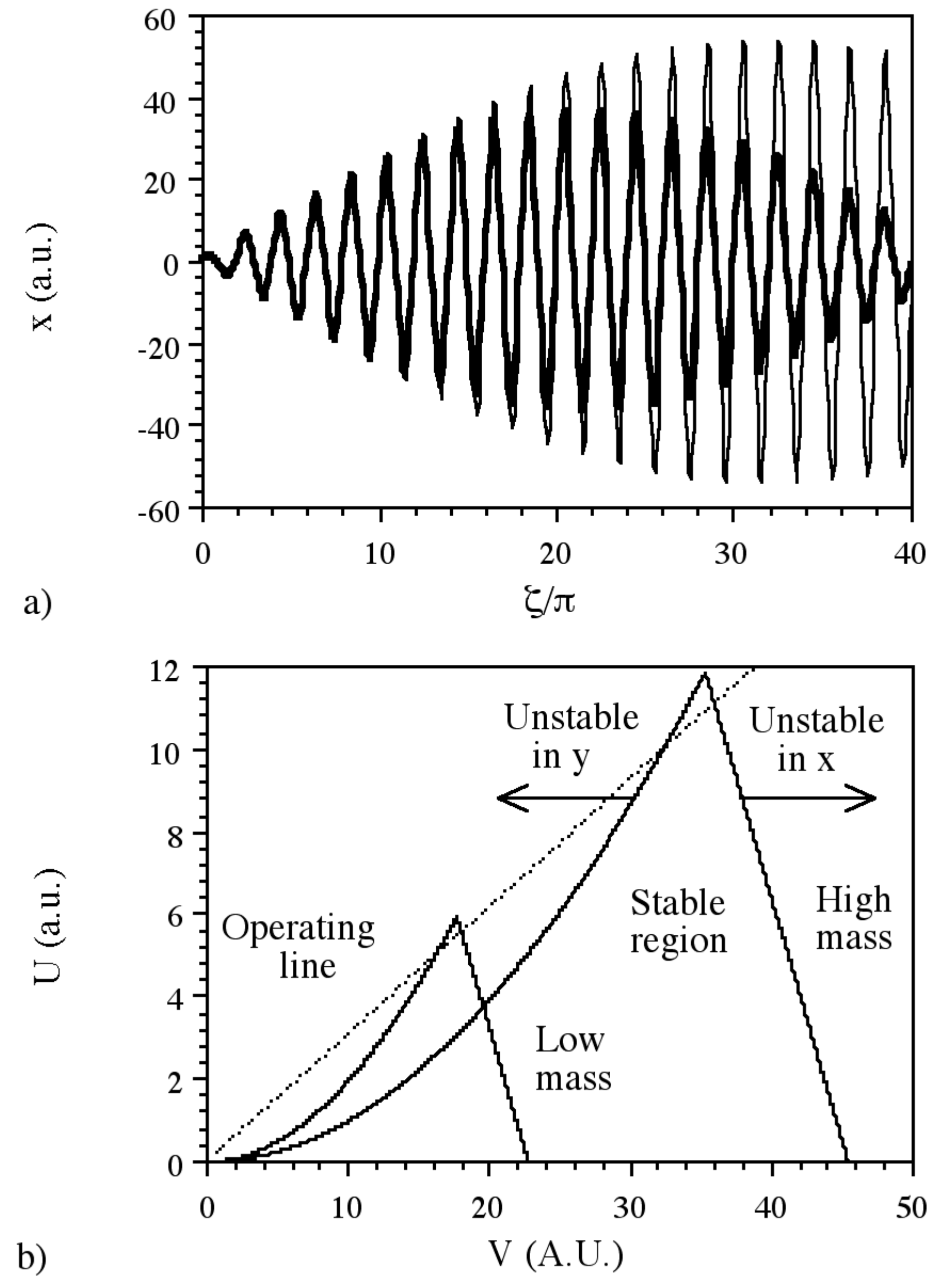
60
40
20
0
-20
-40
-60
x (a.u.)
0
10
20
30
40
ζ/π
a)
12
10
8
6
4
2
0
U (a.u.)
Unstable in y
Unstable in x
Operating line
Stable region
High mass
Low mass
0
10
20
30
40
50
V (A.U.)
b)

Figure 2.

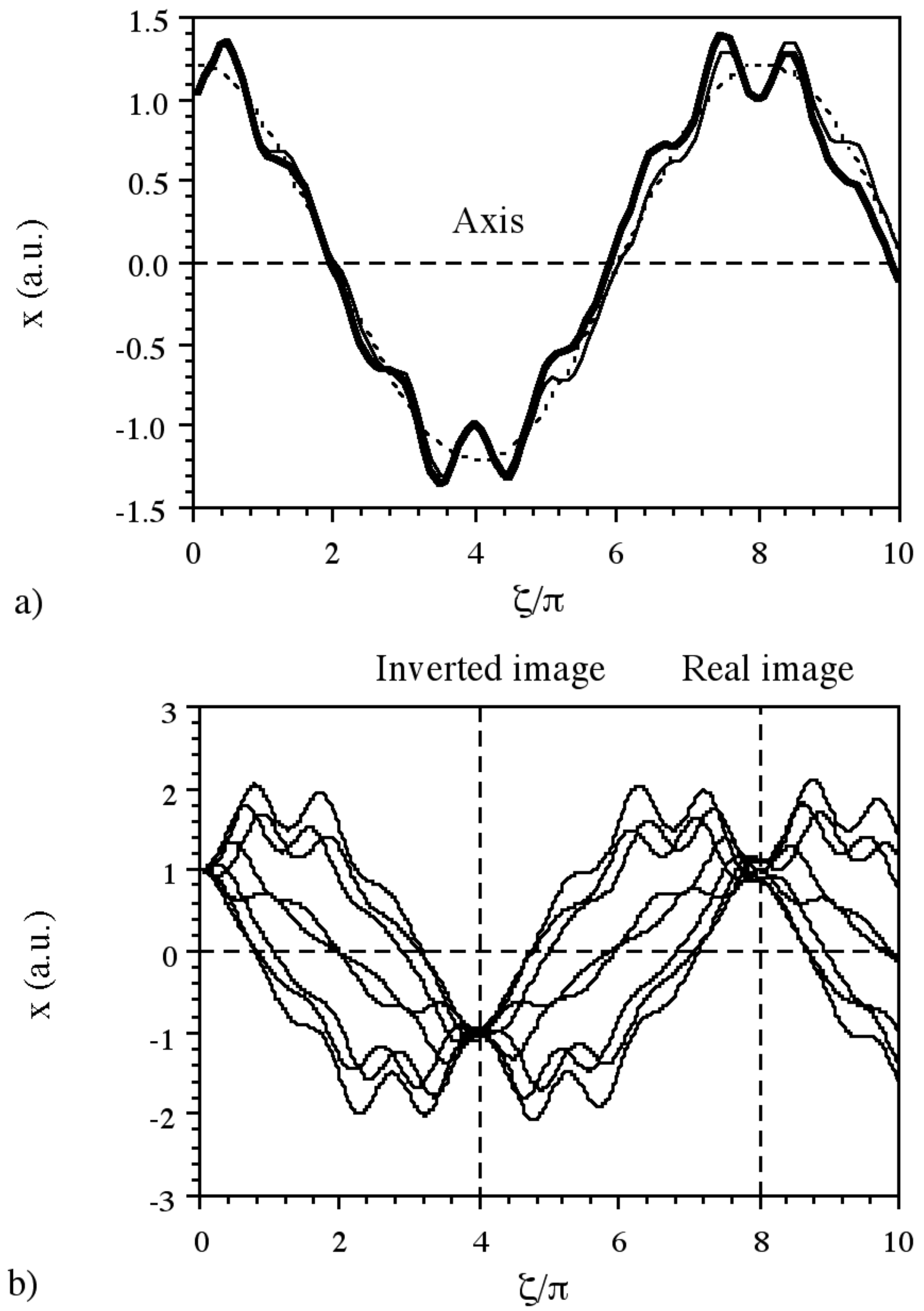
1.5
1.0
0.5
0.0
-0.5
-1.0
-1.5
x (a.u.)
Axis
0
2
4
6
8
10
a)
ζ/π
Inverted image
Real image
3
2
1
0
-1
-2
-3
x (a.u.)
0
2
4
6
8
10
b)
ζ/π

Figure 3.

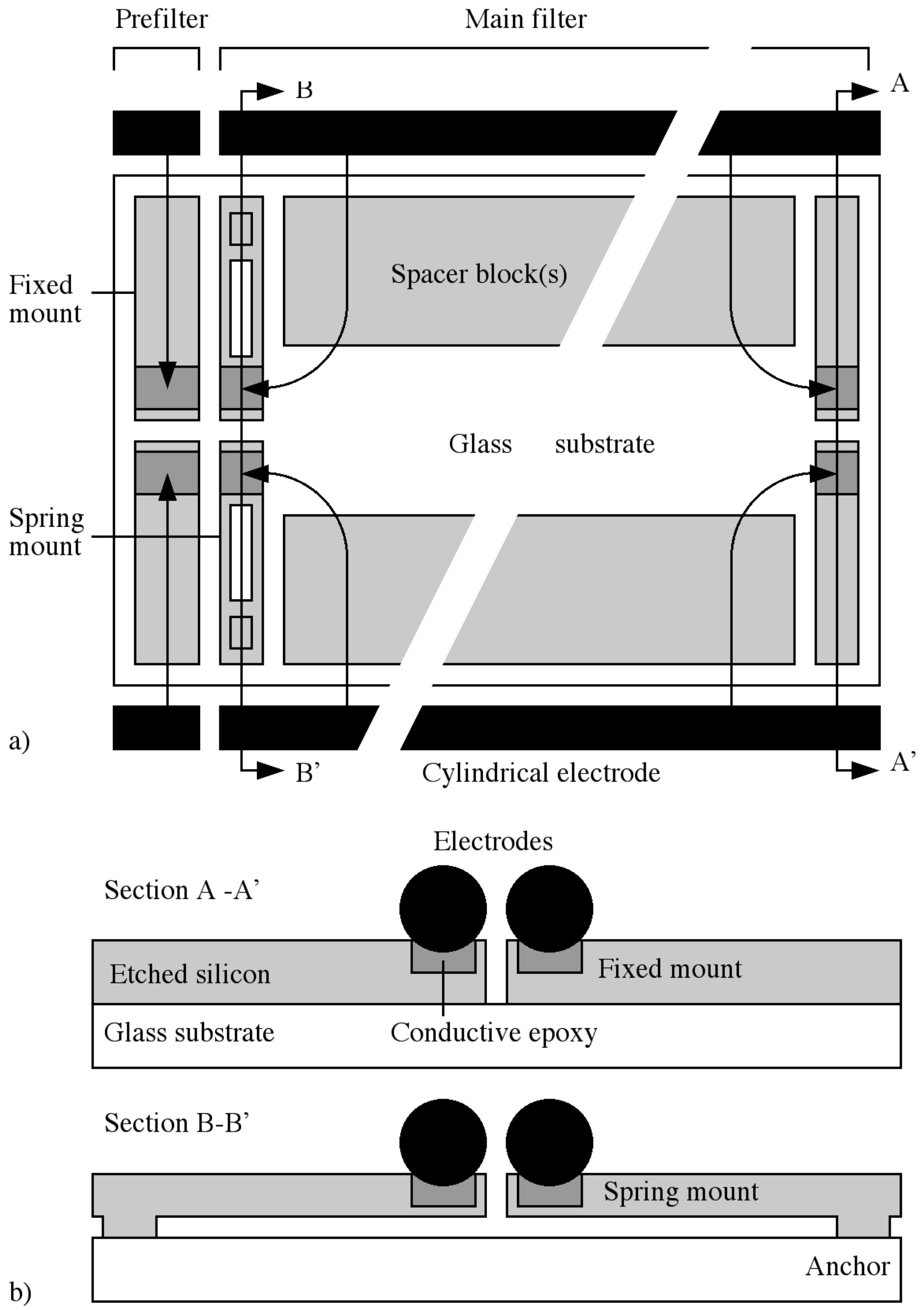
Prefilter
Main filter
B
A
Fixed mount
Spacer block(s)
Glass substrate
Spring mount
a)
B'
Cylindrical electrode
A'
Electrodes
Section A -A'
Etched silicon
Fixed mount
Glass substrate
Conductive epoxy
Section B-B'
Spring mount
Anchor
b)

Figure 4.

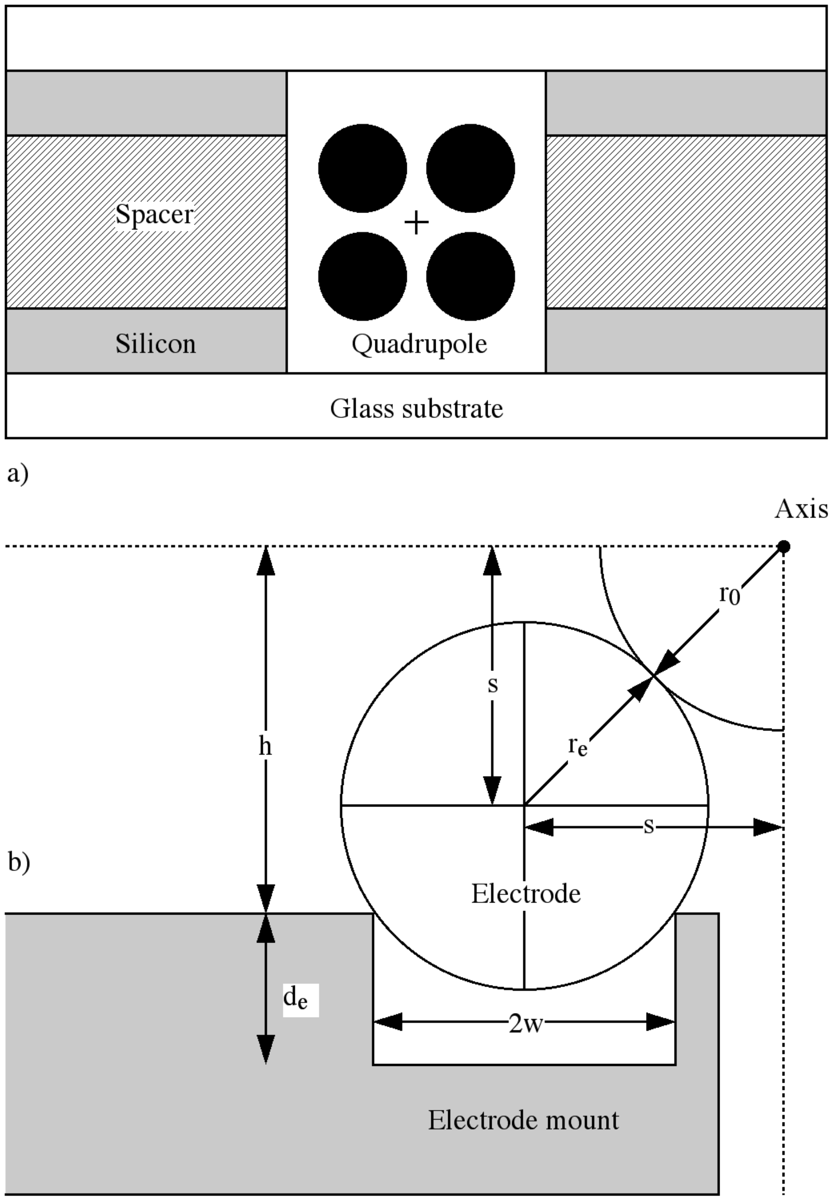
Spacer
Silicon
Quadrupole
Glass substrate
a)
Axis
r_0
h
s
r_e
s
b)
Electrode
d_e
2w
Electrode mount

Figure 5.

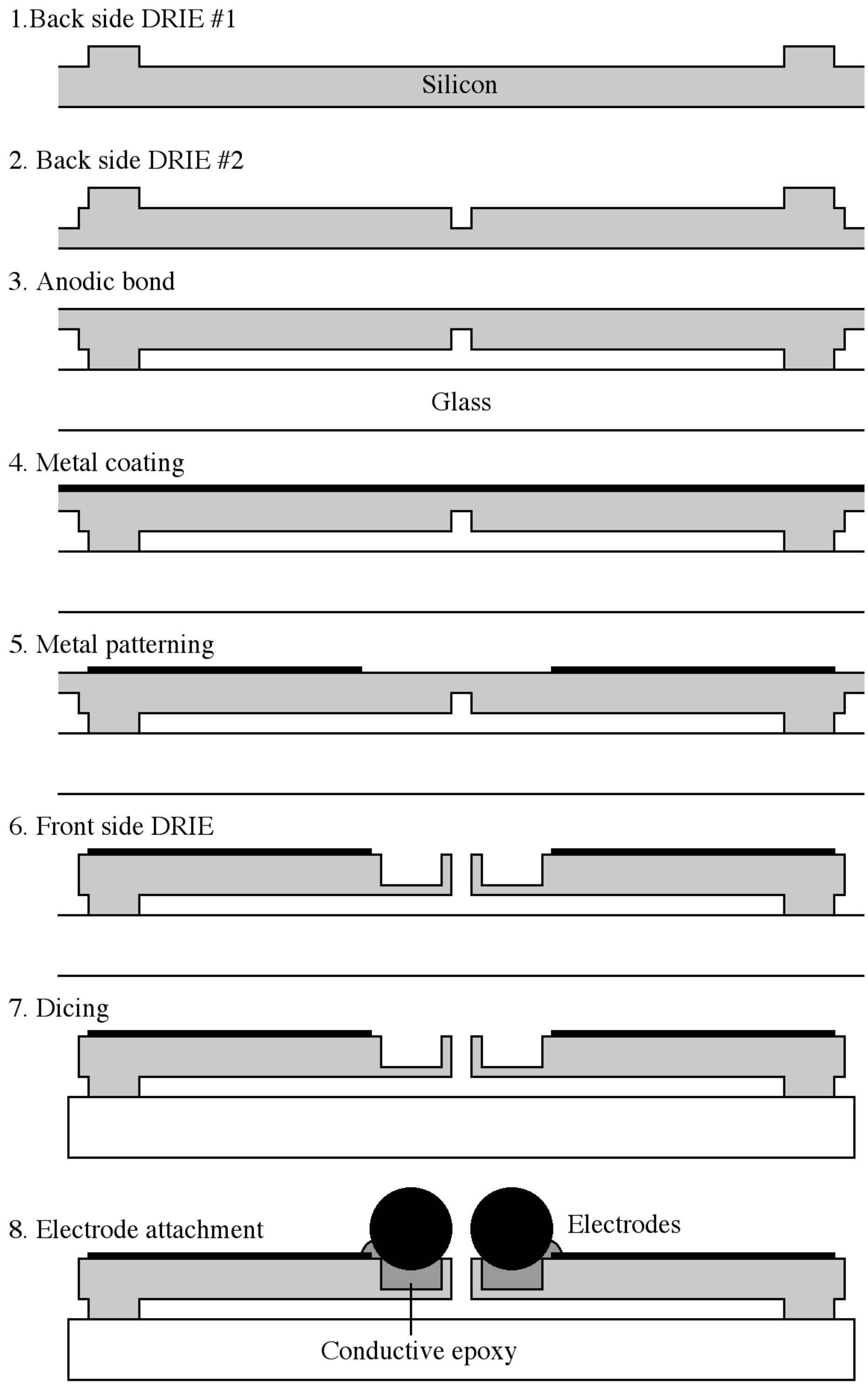
1.Back side DRIE #1
Silicon
2. Back side DRIE #2
3. Anodic bond
Glass
4. Metal coating
5. Metal patterning
6. Front side DRIE
7. Dicing
8. Electrode attachment
Electrodes
Conductive epoxy

Figure 6.

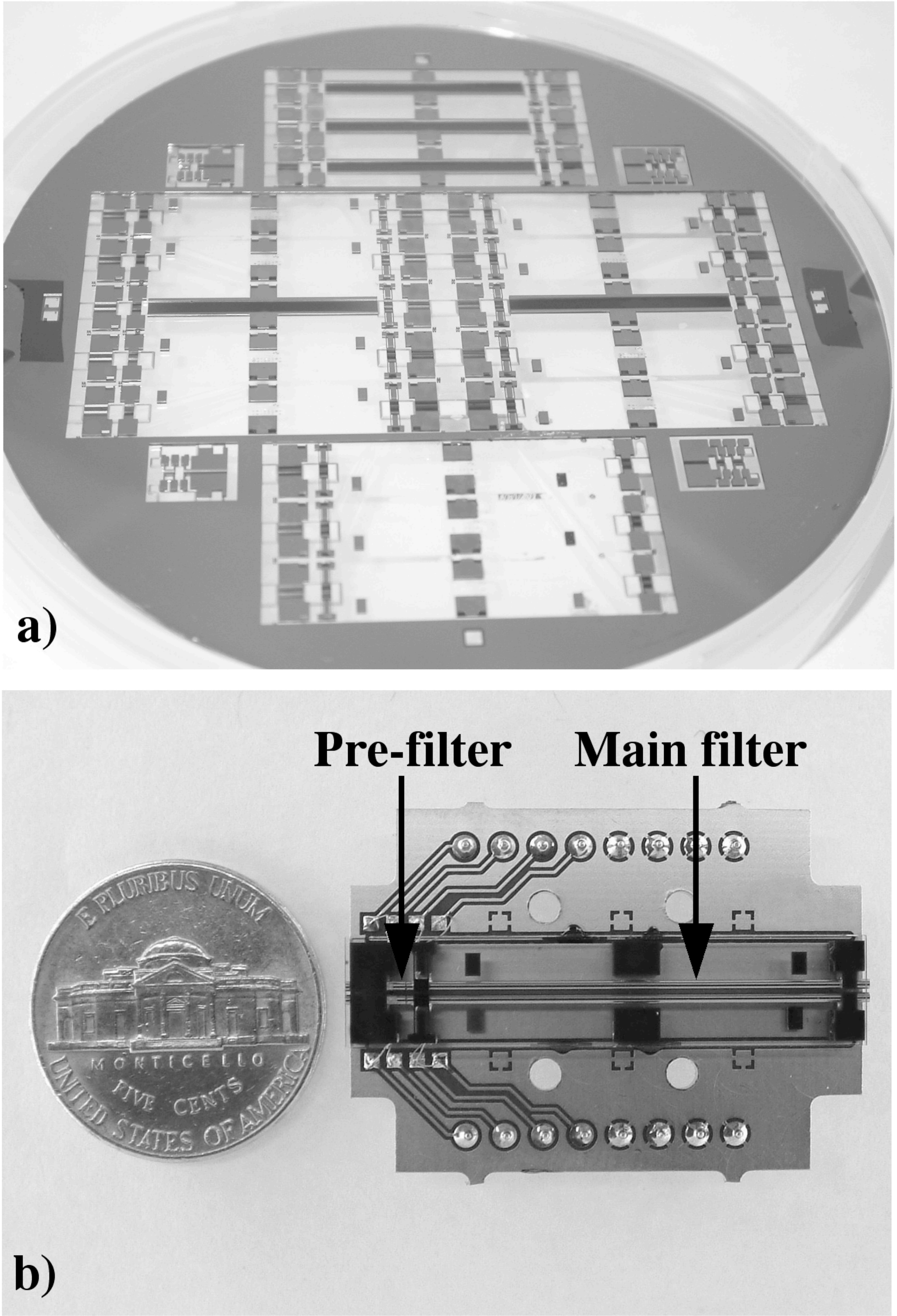
a)
Pre-filter
Main filter
E PLURIBUS UNUM
MONTICELLO
FIVE CENTS
UNITED STATES OF AMERICA
b)

Figure 7.

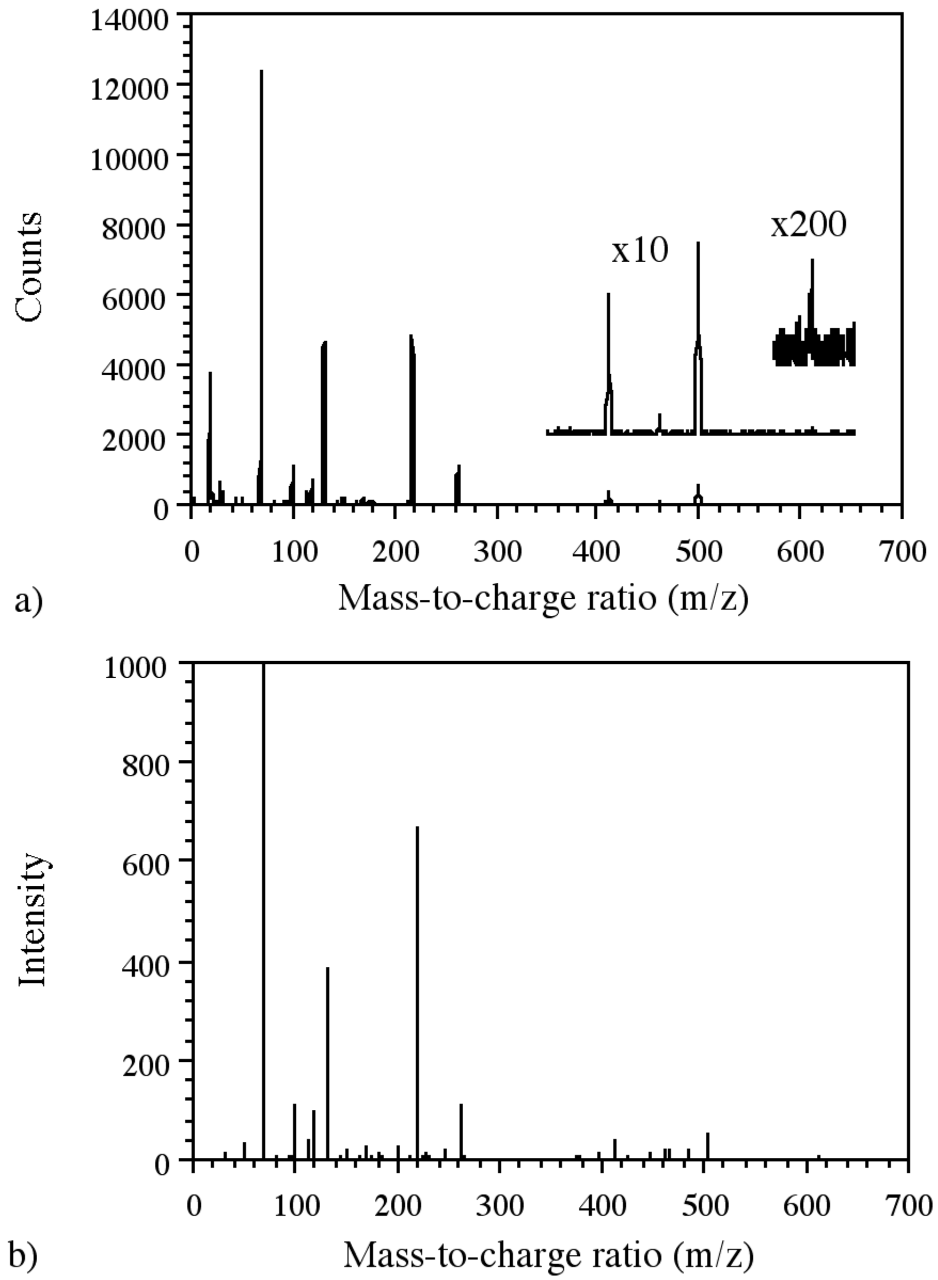
14000
12000
10000
8000
6000
4000
2000
0
Counts
x10
x200
0
100
200
300
400
500
600
700
a)
Mass-to-charge ratio (m/z)
1000
800
600
400
200
0
Intensity
0
100
200
300
400
500
600
700
b)
Mass-to-charge ratio (m/z)

Figure 8.

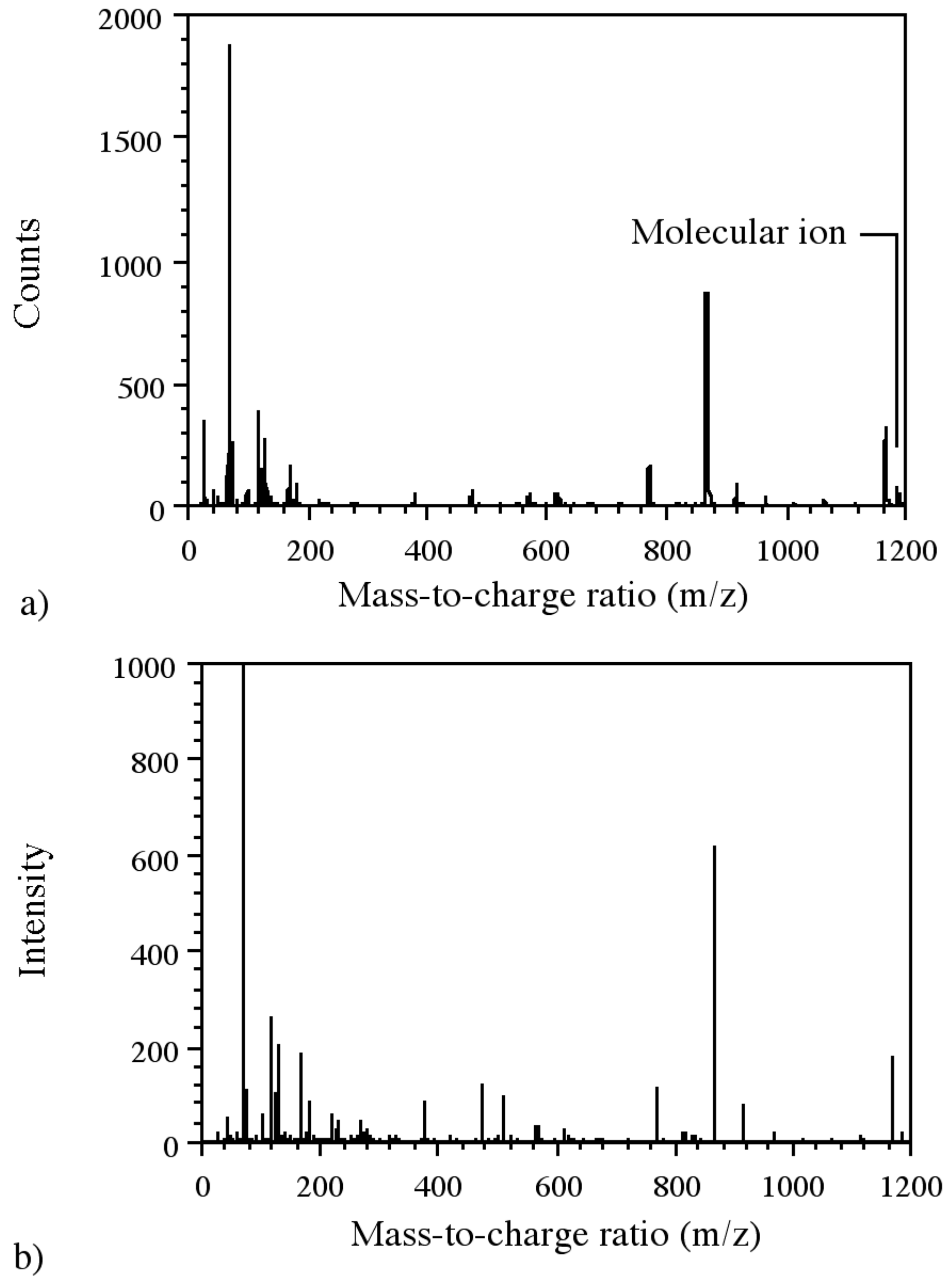
2000
1500
1000
500
0
Counts
Molecular ion
0
200
400
600
800
1000
1200
Mass-to-charge ratio (m/z)
a)
1000
800
600
400
200
0
Intensity
0
200
400
600
800
1000
1200
Mass-to-charge ratio (m/z)
b)

Figure 9.

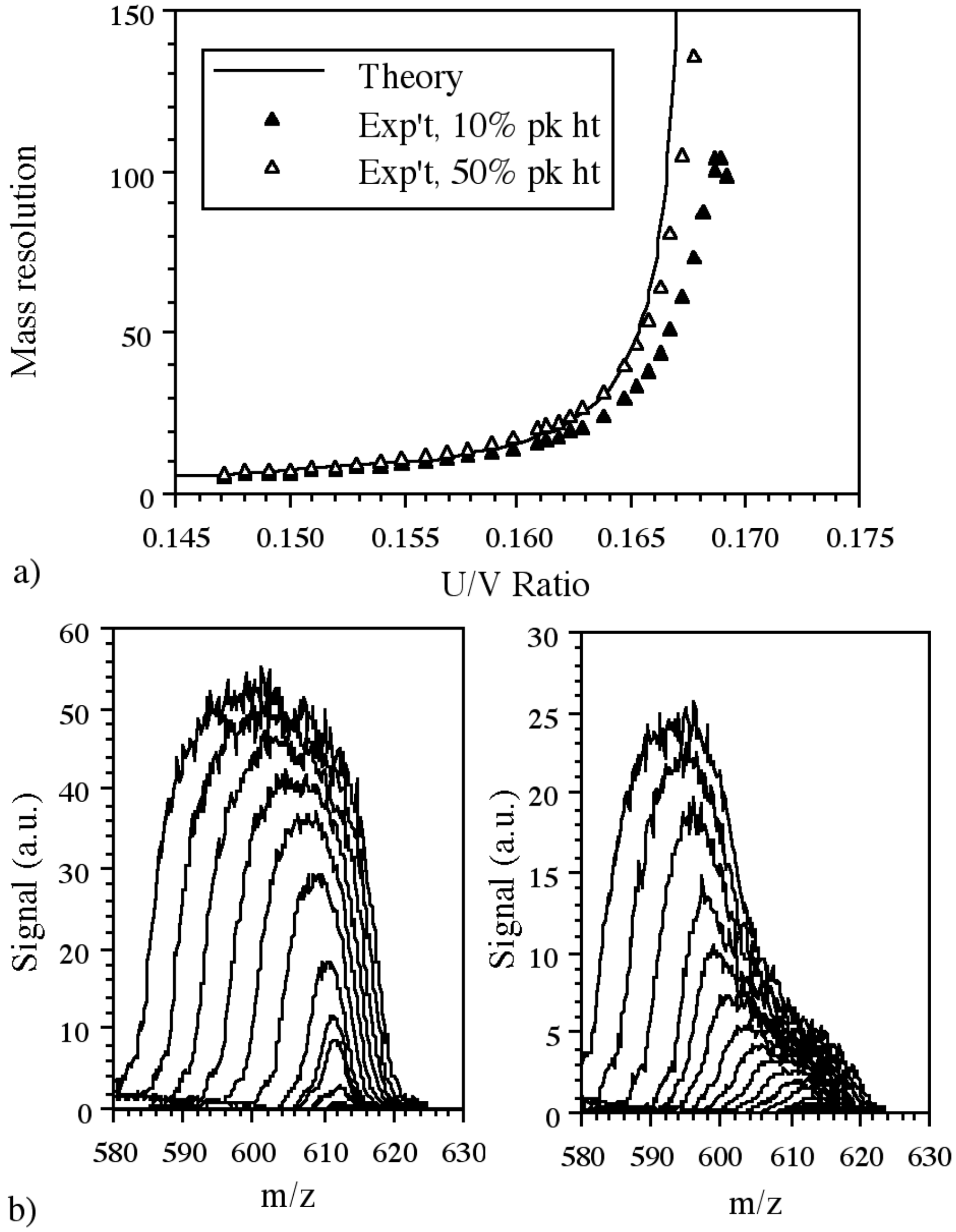
Theory
Exp't, 10% pk ht
Exp't, 50% pk ht
Mass resolution
150
100
50
0
0.145
0.150
0.155
0.160
0.165
0.170
0.175
U/V Ratio
a)
Signal (a.u.)
60
50
40
30
20
10
0
580
590
600
610
620
630
m/z
Signal (a.u.)
30
25
20
15
10
5
0
580
590
600
610
620
630
m/z
b)

Figure 10.

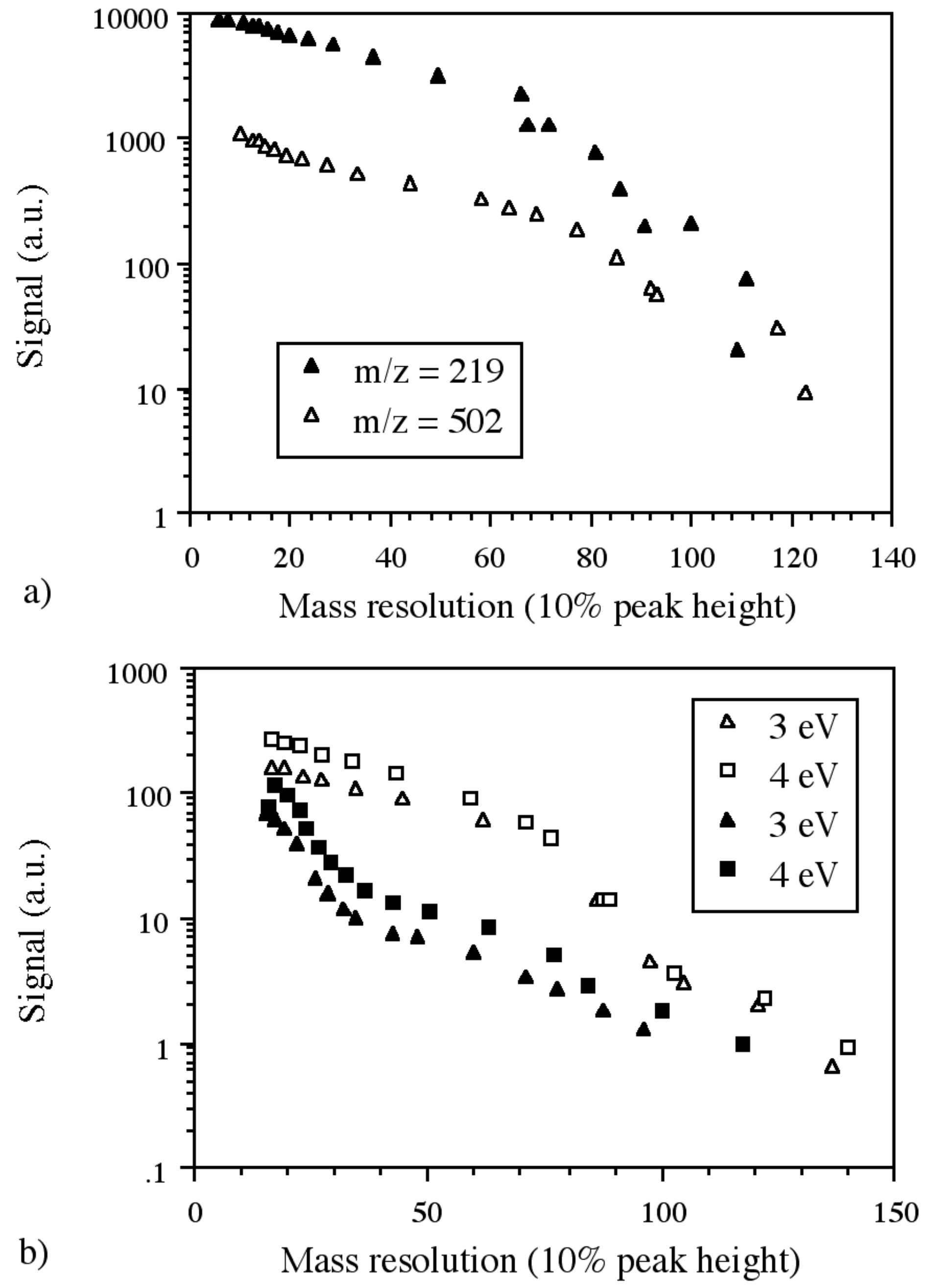
10000
1000
100
10
1
Signal (a.u.)
▲ m/z = 219
△ m/z = 502
0
20
40
60
80
100
120
140
a)
Mass resolution (10% peak height)
1000
100
10
1
.1
Signal (a.u.)
△ 3 eV
□ 4 eV
▲ 3 eV
■ 4 eV
0
50
100
150
b)
Mass resolution (10% peak height)

Figure 11.

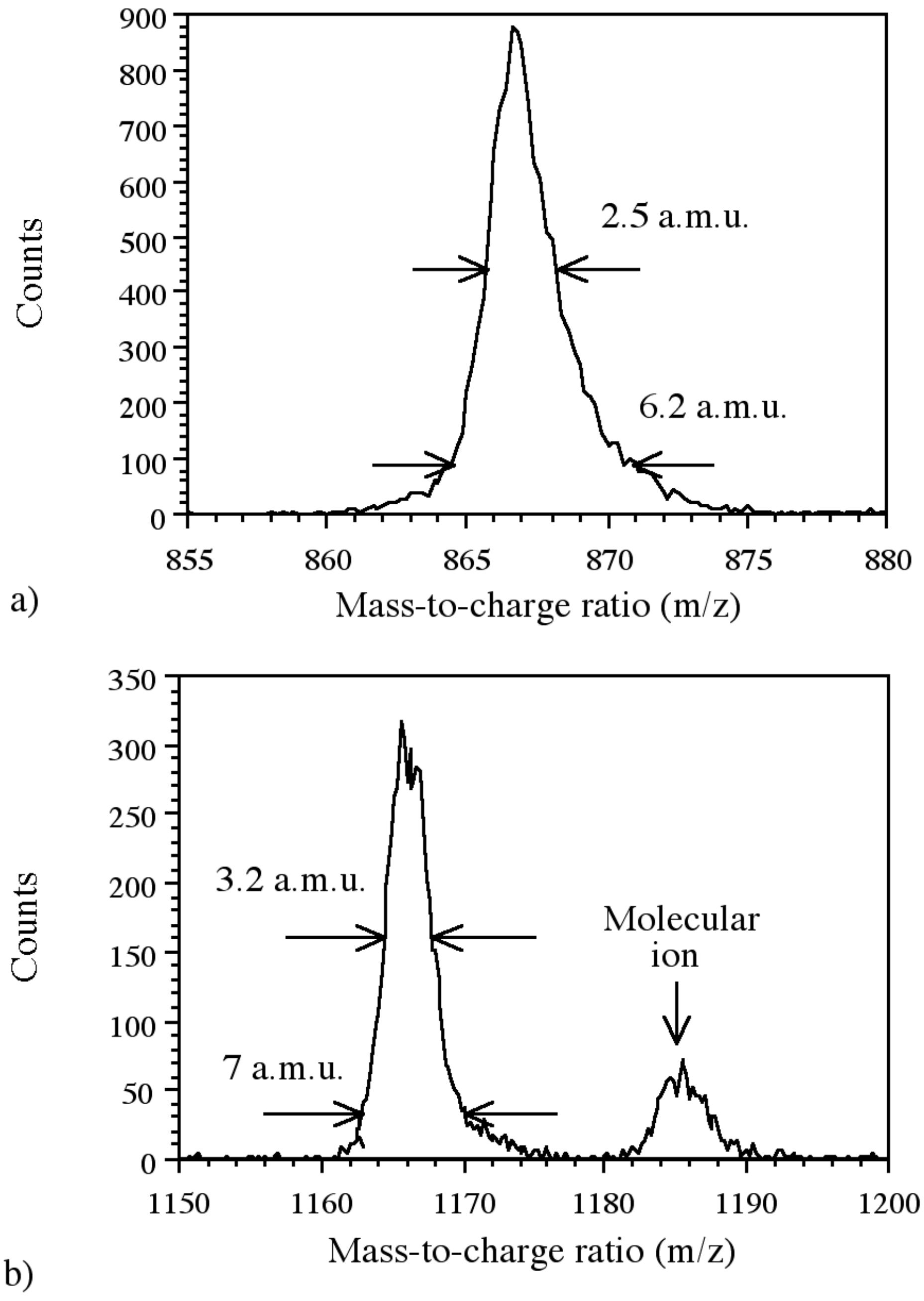
900
800
700
600
500
400
300
200
100
0
Counts
2.5 a.m.u.
6.2 a.m.u.
855
860
865
870
875
880
a)
Mass-to-charge ratio (m/z)
350
300
250
200
150
100
50
0
Counts
3.2 a.m.u.
7 a.m.u.
Molecular ion
1150
1160
1170
1180
1190
1200
Mass-to-charge ratio (m/z)
b)

Figure 12.

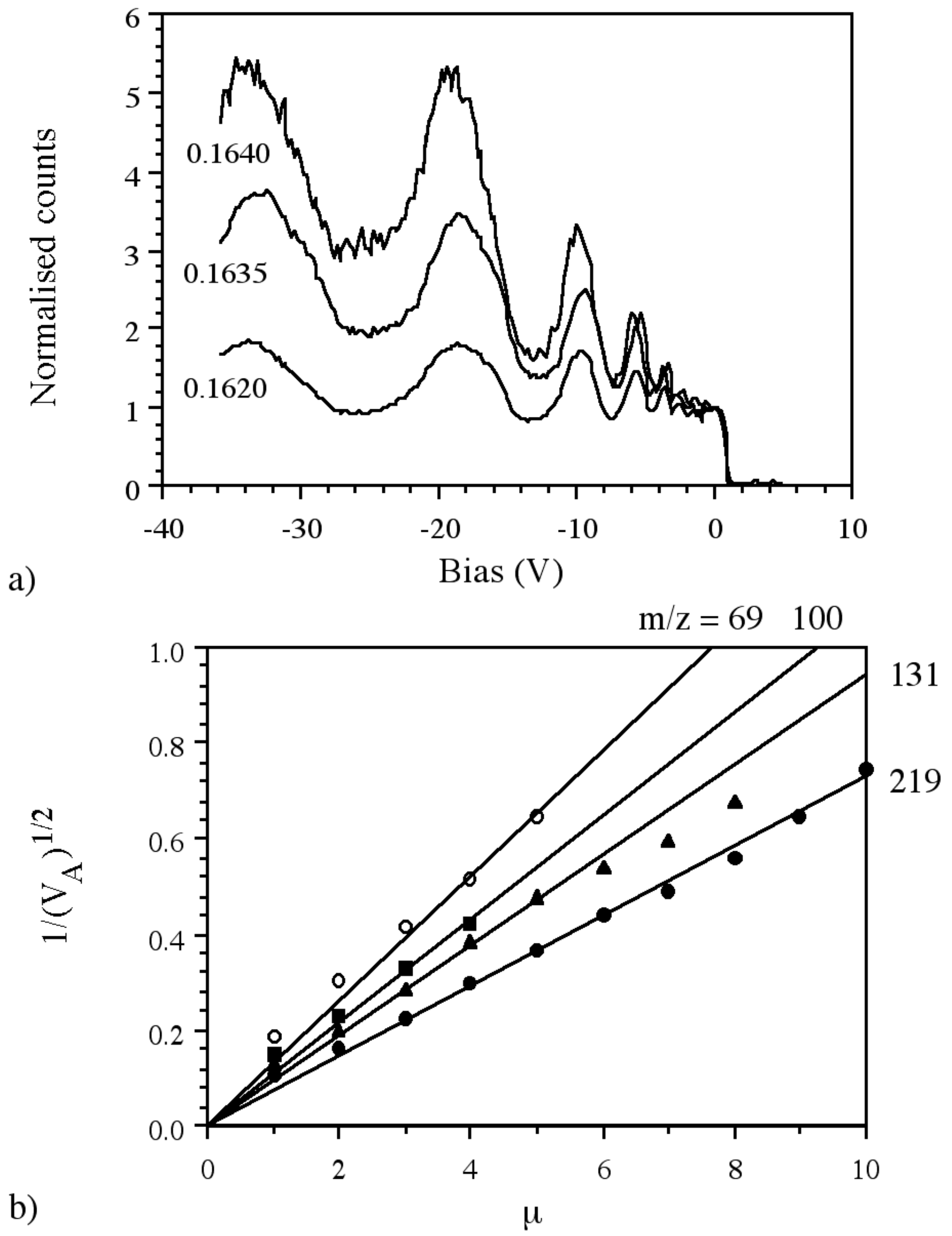
Normalised counts
6
5
4
3
2
1
0
0.1640
0.1635
0.1620
-40
-30
-20
-10
0
10
Bias (V)
a)
m/z = 69
100
131
219
1/(V_A)^{1/2}
1.0
0.8
0.6
0.4
0.2
0.0
0
2
4
6
8
10
μ
b)

Figure 13.